TAR Syndrome-associated Rbm8a deficiency causes hematopoietic defects and attenuates Wnt/PCP signaling

Agnese Kocere[1,2], Elena Chiavacci[2], Kevin Manuel Méndez-Acevedo[3] , Charlotte Soneson[2,4], Max S. Hiltabidle[1], Jacalyn S. MacGowan[5], Daniela Panáková[3,6,7], Margot L. K. Williams[5], Mark D. Robinson[2,4], Christian Mosimann[1], Alexa Burger[1,*]

[1] Department of Pediatrics, Section of Developmental Biology, University of Colorado Anschutz Medical Campus, Aurora

[2] Institute of Molecular Life Sciences, University of Zürich, Zürich, Switzerland

[3] Max Delbrück Center (MDC) for Molecular Medicine in the Helmholtz Association, Berlin-Buch, Germany

[4] Swiss Institute of Bioinformatics (SIB), University of Zürich, Zürich, Switzerland

[5] Center for Precision Environmental Health and Department of Molecular and Cellular Biology, Baylor College of Medicine, Houston

[6] University Hospital Schleswig Holstein, Kiel, Germany

[7] German Centre for Cardiovascular Research (DZHK), partner site Kiel, Germany

* correspondence to: alexa.burger@cuanschutz.edu

ABSTRACT

Defects in blood development frequently occur among syndromic congenital anomalies. Thrombocytopenia-Absent Radius (TAR) Syndrome is a rare congenital condition with reduced platelets (hypomegakaryocytic thrombocytopenia) and forelimb anomalies, concurrent with more variable heart and kidney defects. TAR syndrome associates with hypomorphic gene function for *RBM8A/Y14* that encodes a component of the exon junction complex involved in mRNA splicing, transport, and nonsense-mediated decay. How perturbing a general mRNA-processing factor causes the selective TAR Syndrome phenotypes remains unknown. Here, we connect zebrafish *rbm8a* perturbation to early hematopoietic defects via attenuated non-canonical Wnt/Planar Cell Polarity (PCP) signaling that controls developmental cell arrangements. In hypomorphic *rbm8a* zebrafish, we observe a significant reduction of *cd41*-positive thrombocytes. *rbm8a*-mutant zebrafish embryos accumulate mRNAs with individual retained introns, a hallmark of defective nonsense-mediated decay; affected mRNAs include transcripts for non-canonical Wnt/PCP pathway components. We establish that *rbm8a*-mutant embryos show convergent extension defects and that reduced *rbm8a* function interacts with perturbations in non-canonical Wnt/PCP pathway genes w*nt5b*, *wnt11f2*, *fzd7a*, and *vangl2*. Using live-imaging, we found reduced *rbm8a* function impairs the architecture of the lateral plate mesoderm (LPM) that forms hematopoietic, cardiovascular, kidney, and forelimb skeleton progenitors as affected in TAR Syndrome. Both mutants for *rbm8a* and for the PCP gene *vangl2* feature impaired expression of early hematopoietic/endothelial genes including *runx1* and the megakaryocyte regulator *gfi1aa*. Together, our data propose aberrant LPM patterning and hematopoietic defects as possible consequence of attenuated non-canonical Wnt/PCP signaling upon reduced *rbm8a* function. These results link TAR Syndrome to a potential LPM origin and developmental mechanism.

INTRODUCTION

Mutations in genes that lead to pleiotropic phenotypes, as observed in complex syndromic birth anomalies, remain challenging to mechanistically connect to a tissue- or cell type-specific developmental defect. Thrombocytopenia with absent radius (TAR) Syndrome (OMIM #274000) is a rare (0.42 per 100'000 live births), autosomal-recessive congenital disorder that at birth manifests as blood platelet deficiency (hypomegakaryocytic thrombocytopenia) and bilateral absence of the radius bone (Albers et al., 2013; Petit and Boussion, 2022). While thrombocytopenia is the most consistent phenotype, the limb defects vary considerably among patients and can involve both arms and legs. Concomitant anomalies in TAR syndrome patients can include heart malformations, such as Tetralogy of Fallot or atrial septal defects, floating or unilaterally absent kidneys, as well as mild craniofacial alterations (Albers et al., 2013; Boussion et al., 2020; Greenhalgh, 2002; Klopocki et al., 2007). Curiously, the predominant coagulation defect of newborn TAR patients commonly recedes with age, and patients show normal platelet counts and blood clotting responses a few years after birth (Albers et al., 2013; Petit and Boussion, 2022). The complex combination of organs and cell types affected in TAR patients has so far precluded any clear assignment of a developmental cause underlying the syndrome.

Genetically, *RBM8A* has been identified as causative gene in TAR syndrome patients. Sequence analysis of TAR patients has revealed that compound inheritance of a *1q21.1* deletion that includes *RBM8A* is required with a noncoding single-nucleotide variant in the remaining copy of the *RBM8A* gene (Albers et al., 2012). Corroborating the causal link between TAR Syndrome and *RBM8A*. The major *RBM8A* allele combinations in TAR patients suggest that one gene copy is a complete null by deletion and the other is hypomorphic, while individual patients with bi-allelic *RBM8A* variants in the absence of *1q21.1* deletions have been reported (Albers et al., 2012; Bottillo et al., 2013) (Albers et al., 2012; Albers et al., 2013; Boussion et al., 2020; Petit and Boussion, 2022). *RBM8A* encodes RBM8A/Y14 that together with eIF4A-III, MLN51, and MAGOH constitutes the exon–junction complex (EJC) (Zhao et al., 2000). The EJC is involved in essential post-transcriptional mRNA control by associating with exon-exon junctions after splicing to support nuclear export and sub-cellular localization of specific transcripts, translation enhancement, and nonsense-mediated RNA decay (NMD) (Chuang et al., 2015). NMD as major mRNA quality control step during translation leads to degradation of mRNAs with retained introns as routinely caused by incomplete splicing, in particular of long introns (Ashton-Beaucage et al., 2010; Hir et al., 2015; Kurosaki et al., 2019; Roignant and Treisman, 2010). Which mechanism(s), mRNA target(s), and developmental process(es) are affected in TAR Syndrome upon reduced RBM8A function remain unknown.

Pioneering work on recessive zebrafish *rbm8a* and *magoh* mutants has documented the impact of EJC perturbation in which maternal mRNA and protein contribution to the embryo rescues development until lack of zygotic supply causes aberrant phenotypes (Gangras et al., 2020). Zygotic *rbm8a* loss-of-function resulted in no discernible morphological phenotypes until late segmentation stages (approximately 19 hpf), when cell death in the brain and general muscle paralysis became detectable (Gangras et al., 2020). Notably, zebrafish *rbm8a* mutants showed disrupted NMD and increased stability of mRNAs with 3' UTR introns by 24 hpf (Gangras et al., 2020). In *Drosophila*, tissue-specific disruption of NMD using *rbm8a* and *magoh* mutants has been linked to

accumulation of individual mRNAs with retained large introns that result in perturbation of select developmental processes such as RAS/MAPK signaling (Ashton-Beaucage et al., 2010; Roignant and Treisman, 2010). Together, these data document both quantitative as well as qualitative impact on individual mRNAs upon EJC perturbation in different models.

A possible lead to connect the seemingly pleiotropic TAR Syndrome phenotypes comes from the developmental origin of the affected organs. The lateral plate mesoderm (LPM) forms the progenitor cells for blood, heart, vasculature, kidney, craniofacial muscles, and limb connective tissue in the developing vertebrate embryo (Davidson and Zon, 2004; Garcia-Martinez and Schoenwolf, 1992; Onimaru et al., 2011; Schier and Talbot, 2005; Schoenwolf et al., 1992). Hypomorphic perturbation of *RBM8A* in TAR Syndrome could therefore impact genes involved in a shared developmental process at the base of blood, limb, heart, and kidney development. The diversity of LPM cell fates could explain complex, yet developmentally connected co-morbidities of syndromic congenital anomalies as LPM diseases that result from early patterning defects (Kocere et al., 2023). By affecting blood, forelimbs, heart, and kidneys, the spectrum of TAR syndrome phenotypes seems to predominantly affect tissues of LPM origin (**Fig. 1A**). Yet, what developmental mechanisms altered RBM8A/Y14 dosage in TAR Syndrome triggers to possibly cause a LPM defect, and in particular thrombocytopenia, remains unknown.

Hematopoietic progenitor cells emerge in close association with endothelial progenitors within the LPM, starting with a first wave of *Gata1*-expressing primitive erythrocytes. Subsequent intermediate hematopoietic progenitors form primitive myeloid cells including transient megakaryocytes that in mammals begin to shed thrombocytes (also called platelets) for coagulation (Bianchi et al., 2016; Machlus and Italiano, 2013; Tober et al., 2007; Trowbridge et al., 2006). The *Runx1*-expressing hematopoietic stem cell (HSC) precursors emerge from the ventral wall of the dorsal aorta and undergo various maturation steps before seeding the final hematopoietic niches (Chen et al., 2009; Gao et al., 2018; Kissa and Herbomel, 2010; Yzaguirre et al., 2017). Definitive megakaryocytes emerge from HSC-derived common myeloid progenitors that also form erythrocytes plus mast cells and myeloblasts. The Gfi1 transcription factors have been implicated in controlling hematopoietic lineage progression in human and mouse: Gfi1b predominantly drives megakaryocyte differentiation by suppressing erythroid fate, with missense mutations in human *GFI1B* causing thrombocytopenia (Beauchemin and Möröy, 2020; Cheng et al., 2019; Saleque et al., 2002). In zebrafish, the orthologs *gfi1aa* and *gfi1b* contribute to primitive erythropoiesis and are expressed in erythroid, intermediate erythroid-myeloid progenitors (EMPs), and emerging hematopoietic stem cells (Cooney et al., 2013; Moore et al., 2018; Thambyrajah et al., 2016). At which step embryonic perturbation of Rbm8a affects thrombocyte formation and how it connects to the other LPM-associated defects awaits clarification.

Here, harnessing the dosage range provided by maternal contribution, different mutant *rbm8a* alleles, and antisense morpholino knockdown in zebrafish, we investigate if Rbm8a perturbation akin to TAR Syndrome causes the thrombocytopenia phenotype and further affects early steps in LPM patterning. We provide evidence

that reduced *rbm8a* function causes intron retention and misexpression of mRNAs encoding components of the non-canonical Wnt/PCP pathway involved in embryo axis elongation through convergence and extension movements. Subsequently, *rbm8a* attenuation results in several, cumulatively significant defects in early LPM and endothelial/hematopoietic lineage patterning that we also document in embryos with classic PCP defects. Our data connect impaired PCP signaling with hematopoietic phenotypes as possible developmental origin of the phenotypes observed in TAR Syndrome.

RESULTS

Null and hypomorphic *rbm8a* perturbation in zebrafish

Previous work has established that zebrafish *rbm8a* is maternally contributed as mRNA and protein, persisting for at least 24 hpf (Gangras et al., 2020). This waning maternal contribution has been used to assess hypomorphic and loss-of-function phenotypes from 19 hpf on, yet *rbm8a*-mutant embryos deteriorate rapidly past 24-28 hpf and are severely deformed by 72 hpf (Gangras et al., 2020). We therefore sought genetic means to decrease Rbm8a protein levels to establish hypomorphic Rbm8a function beyond these timepoints.

To generate mutant alleles, we targeted the zebrafish *rbm8a* locus by CRISPR-Cas9 mutagenesis to induce non-homologous end joining (NHEJ)-mediated lesions in the coding sequence (**Fig. 1B**). We raised surviving low-dose crispants and isolated two different mutant *rbm8a* alleles: *g.5152_5156del* and *rbm8a g.5152_5154del*, subsequently abbreviated as *rbm8a*$^{\Delta 5}$ and *rbm8a*$^{\Delta 3}$, respectively (**Fig. 1B**). *rbm8a*$^{\Delta 5}$ is a frameshift allele with no downstream alternative start codons that likely represents a null allele (**Fig. 1B**); no Rbm8a protein is detected by Western Blot at 24-26 hours post-fertilization (hpf) after the considerable maternal mRNA and protein deposition subsides (**Fig. 1C, Supplemental Fig. 1**). Notably, our independently isolated allele is molecularly identical to the allele previously reported by Gangras and colleagues and generated with the same recommended sgRNA sequence, indicating preferential repair of this lesion with a 5 bp deletion (Gangras et al., 2020). In contrast, our additional allele *rbm8a*$^{\Delta 3}$ deleted three base pairs, replacing *phenylalanine* (*F*) and *proline* (*P*) codons with a single *serine* (*S*) codon, substituting two non-polar side chains with a polar OH group (**Fig. 1B**). *rbm8a*$^{\Delta 3}$ substitutes amino acids right before the first alpha-helix in the Rbm8a N-terminus that is in proximity with the beta-sheet in Magoh (Bono et al., 2006; Fribourg et al., 2003; Shi and Xu, 2003), proposing *rbm8a*$^{\Delta 3}$ as potential hypomorphic allele.

Embryos heterozygous for either allele (*rbm8a*$^{\Delta 3/+}$ and *rbm8a* $^{\Delta 5/+}$) showed no obvious malformations at observed timepoints up to 5 days post-fertilization and adults were viable and fertile (**data not shown**). As previously reported and compared to wildtype siblings, homozygous *rbm8a*$^{\Delta 5}$ (*rbm8a*$^{\Delta 5/\Delta 5}$) zebrafish developed seemingly normal for the first 19 hpf, with subtle axis shortening during segmentation, before rapidly developing severe body axis hypoplasia (**Fig. 1D**). Around 26 hpf, the embryos started to display hypoplastic heads and tails with twisted axis, yet featured slowed heartbeat and rudimentary circulation before progressively deteriorating without survival past 60-72 hpf (**Fig. 1D**). In contrast, homozygous *rbm8a*$^{\Delta 3}$ (*rbm8a*$^{\Delta 3/\Delta 3}$) embryos

developed and survived without obvious overt defects into fertile adults (**Fig. 1D**) . By crossing, we derived trans-heterozygous *rbm8a*$^{\Delta5/\Delta3}$ embryos that harbor one allele as likely null while the other provides hypomorphic activity; *rbm8a*$^{\Delta5/\Delta3}$ embryos resembled wildtype siblings during early development and continued to develop seemingly normal until adulthood. Incrosses of adult *rbm8a*$^{\Delta5/\Delta3}$ resulted in the expected phenotypes and allele combinations, as observed in heterozygous incrosses of the individual alleles.

To further control embryonic Rbm8a protein levels, we obtained the translation-blocking morpholino *MO-rbm8aATG*. Injection of 1 nL of 0.01 nmol/µL *MO-rbm8aATG* phenocopied *rbm8a*$^{\Delta5/\Delta5}$ embryos by morphology (**Fig. 1D**). Morpholino injection also resulted in rapid translation block and reduction of Rbm8a protein already at tailbud stage and absence by 17 hpf, as detected by Western blot (**Fig. 1C, Supplemental Fig. 1**). Co-injection of *MO-rbm8aATG* with capped mRNA encoding human *RBM8A* that has no sequence overlap with the morpholino rescued the knockdown embryos to at least 5 dpf, while *EGFP* mRNA as control had no rescue capacity (**Supplemental Fig. 2A-G, Supplemental Table 1**). Together, these data validate *MO-rbm8aATG* as complementary tool to our *rbm8a* allelic series.

Altogether, these reagents establish a zygotic-mutant allelic series of zebrafish *rbm8a* and a potent translation-blocking knockdown reagent to study the impact of *rbm8a* perturbations on early development, recapitulating aspects of TAR genetics (**Supplemental Fig. 2H, Supplemental Table 1**).

Hypomorphic *rbm8a* results in thrombocyte reduction

The functional equivalent of cytoplasmic platelets shed by megakaryocytes in humans, nucleated thrombocytes in zebrafish are labeled by the transgenic reporter *cd41:EGFP* starting from 40-46 hpf (Belmonte et al., 2021; Lin et al., 2005). Notably, *cd41:EGFP* transgenics harbor EGFP-high thrombocytes and EGFP-low prospective hematopoietic stem cell precursors (HSPCs) that can be distinguished by sorting and fluorescence imaging (Bertrand et al., 2008; Gansner et al., 2017). As *rbm8a* $^{\Delta5/\Delta5}$ mutants and *MO-rbm8aATG* morphants deteriorate beyond 28-30 hpf (**Fig. 1D**), we sought to test thrombocyte numbers in genetic combinations with the hypomorphic *rbm8a*$^{\Delta3}$ allele. We additionally established an injection titration curve for *MO-rbm8aATG* to reduce Rbm8a protein levels and to maintain viability: the suboptimal dose ranged between 1:125 and 1:150 stock dilution and resulted in slight to no detectable developmental defects in the morphants with survival beyond 7 dpf, compared to a dose of 1:100 that fully phenocopied *rbm8a*$^{\Delta5/\Delta5}$ mutants (**Fig. 1D**).

We quantified thrombocytes in controls and upon mutant and morpholino-induced *rbm8a* perturbation in *cd41:EGFP*-transgenic larvae at 3 dpf and 6 dpf, when thrombocytes are clearly detectable. To transiently arrest the heartbeat and stop circulation, we treated the larvae with 2,3-Butanedione monoxime (BDM) and quantified EGFP-positive cells from fluorescent images of whole larvae using custom Fiji scripts (**Fig. 2A**). This approach provided a semi high-throughput quantification to distinguish the circulating, high EGFP-expressing thrombocytes from the immobile, sparser low EGFP-expressing HSPCs in the caudal hematopoietic territory

(CHT) (**Fig. 2A-I**). Our quantification documented a significant decrease in the number of high EGFP-positive cells at both 3 and 6 dpf in the morphants with a clear response to the dose of morpholino compared to wildtype animals (**Fig. 2B-E,J,K, Supplemental Table 2**). Notably, viable mutant allele combinations for *rbm8a* showed no significant change to *cd41:EGFP*-expressing cell numbers at 3 dpf (**Fig. 2F,H,J, Supplemental Table 2**), in line with unperturbed maternal deposition of *rbm8a* mRNA and translated protein (**Fig. 1C**) (Gangras et al., 2020). In contrast, at 6 dpf, *rbm8a*$^{\Delta 3}$-homozygous larvae showed a significant reduction of *cd41:EGFP* cell counts, while *rbm8a*$^{\Delta 3/\Delta 5}$ larvae showed an even further reduction (**Fig. 2G,I,K, Supplemental Table 2**). This reduction was significant in larvae derived from incrosses of *rbm8a*$^{\Delta 3/\Delta 5}$ parents in which the oocytes only harbor the hypomorphic *rbm8a* allele as functional copy, further underlining the influence of maternally contributed wildtype *rbm8a* transcript. These data are in line with a potential hypomorphic quality of the *rbm8a*$^{\Delta 3}$ allele.

Taken together, using our available genetic tools, these observations indicate that *rbm8a*-perturbed larvae show reductions in thrombocyte numbers that are dependent on functional Rbm8a levels.

rbm8a perturbation impairs mRNAs encoding planar cell polarity components

To identify developmental mechanisms influencing thrombocyte formation and general hematopoiesis upon *rbm8a* perturbation, we sought to define the transcriptome of *rbm8a*-mutant zebrafish embryos at early developmental stages. Prior work has described the transcriptome of 21 hpf and 27 hpf *rbm8a*$^{\Delta 5/\Delta 5}$ embryos, when mutants show clear signs of deterioration including onset of widespread apoptosis and necrosis (Gangras et al., 2020). We therefore analyzed the transcriptome of tailbud (9 hpf) *rbm8a*$^{\Delta 5/\Delta 5}$ embryos as well as 24 hpf as comparison, capturing with the former the end of gastrulation when maternal Rbm8a protein and *rbm8a* mRNA levels start to wane (**Fig. 3 A-C**). The RNA-seq data can be browsed in our R/Shiny-based app RNA-seq Explorer with an interactive interface (http://imlspenticton.uzh.ch:3838/mosimann_p2452/; see Methods for details).

Comparing *rbm8a*$^{\Delta 5/\Delta 5}$ versus wildtype embryos, we identified 850 differentially expressed genes (720 of which were protein coding) with FDR <= 0.05 at tailbud stage (**Supplemental Table 3**), and 1988 genes (1818 of which were protein-coding) with FDR <= 0.05 at 24 hpf (**Supplemental Table 4**) (**Fig. 3B,C**). We used Metascape (Zhou et al., 2019) to identify statistically enriched functional annotations of deregulated genes and their accumulative hypergeometric p-values (**Supplemental Fig. 3A,B, Supplemental Table 5**): similar to the reported transcriptomes of 21 and 27 hpf *rbm8a*$^{\Delta 5/\Delta 5}$ embryos (Gangras et al., 2020), at 24 hpf we observed enrichment for cell death and responses to stress among the upregulated genes, as well as downregulation of cell cycle processes and chromatin organization (**Supplemental Fig. 3A,B, Supplemental Table 5**). These transcriptional changes are in line with the progressive deterioration of *rbm8a*$^{\Delta 5/\Delta 5}$ embryos as visible by the mutant and morphant phenotypes at that stage (**Fig. 1**) (Gangras et al., 2020). In contrast, at tailbud stage, we observed broad deregulated gene categories associated with morphogenesis and general organ development (**Supplemental Fig. 3A,B, Supplemental Table 5**).

As part of the EJC, Rbm8a functions in NMD that removes mRNAs with retained introns or other splicing defects that occur routinely during native post-transcriptional processing (Hir et al., 2015; Kurosaki et al., 2019; McMahon et al., 2016; Palacios et al., 2004). In *Drosophila*, loss of *rbm8a* causes selective retention of mRNAs with mis-spliced large introns due to defective NMD (Ashton-Beaucage et al., 2010; Roignant and Treisman, 2010), and previous analysis of zebrafish *rbm8a* mutants documented stabilization of mRNAs with introns in their 3' UTRs (Gangras et al., 2020). Together, these data document both quantitative as well as qualitative impact on individual mRNAs upon EJC perturbation in different models. Given the depth of sequencing and early versus late timepoint in our dataset, we next asked if qualitative differences in individual transcripts could link Rbm8a deficiency with TAR Syndrome-associated processes.

We therefore scanned the tailbud stage and 24 hpf transcriptome of *rbm8a*-mutant embryos for differential exon and intron usage of individual mRNAs using DEXSeq (**Supplemental Fig. 3C**) (Anders et al., 2012). After filtering (retaining only protein-coding transcripts and further excluding U12 splice introns, transcripts with read counts below 100, adjusted p value per gene <= 0.05 and differential exon/intron usage event <= 0.1), we found 697 differential intron usage events in 564 genes (**Supplemental Table 6**) and 713 differential exon usage events in 502 genes (**Supplemental Table 7**) in *rbm8a*$^{\Delta 5/\Delta 5}$ mutants compared to wildtype at tailbud stage (**Supplemental Fig. 3C**). In contrast, and again in line with progressive deterioration, we found 2220 differential intron usage events in 1594 genes (**Supplemental Table 6**) and 5439 differential exon usage events in 2316 genes (**Supplemental Table 7**) in *rbm8a*$^{\Delta 5/\Delta 5}$ compared to wildtype at 24 hpf (**Supplemental Fig. 3C**). This analysis reveals a considerable qualitative difference in numerous mRNAs following *rbm8a* perturbation in zebrafish, including mRNAs with retained introns. Curiously, most of the retained introns were larger than 1 kb at bud stage, compared to retained introns of all sizes at 24 hpf when the *rbm8a*$^{\Delta 5/\Delta 5}$ embryos were declining (**Fig. 3D**).

Among irregular transcripts with developmental contributions at both analyzed stages, we found several mRNAs encoding components of the non-canonical Wnt pathway involved in planar cell polarity (PCP) signaling, including *celsr2*, *wnt5b*, *wnt11f2* and *vangl2* (**Fig. 3E-G, Supplemental Fig. 3D**). PCP signaling equips tissues with a polarity axis resulting in collective morphogenetic events, such as the orientation of subcellular structures and cell rearrangements (Butler and Wallingford, 2017). These mRNAs showed variable, yet considerable sequencing reads in individual introns, indicating seemingly minor but significant accumulation of mis-spliced transcripts with retained introns (**Fig. 3E-G, Supplemental Fig. 3D**). Such intron retention is predicted to lead to unproductive protein translation or truncated, functionally perturbed polypeptides (Hir et al., 2015; Kurosaki et al., 2019), potentially lowering the effective dose of individual non-canonical Wnt/PCP components. We also noted that one transcript isoform of *celsr2*, encoding one of several Flamingo family receptors for non-canonical Wnt/PCP ligands (Butler and Wallingford, 2017; Joshi et al., 2022), was among the top-upregulated mRNAs at tailbud stage in *rbm8a*$^{\Delta 5/\Delta 5}$ embryos (logFC 10.4, FDR=0.013); at 24 hpf, *celsr2* mRNAs showed selective intron retention of intron 15 (logFC 2.4, p=0.00015) (**Fig. 3B,C, Supplemental Fig. 3D**). Transcripts of the key PCP component *vangl2* showed differential variant use between our sequenced timepoints (**Fig. 3G,H**).

Taken together, our analysis indicates that *rbm8a*-mutant embryos already show developmental anomalies at the bulk transcriptome level at the end of gastrulation, when maternal *rbm8a* mRNA and Rbm8a protein contribution is starting to fade. From our qualitative assessment of mRNAs at tailbud and 24 hpf stage, we hypothesized that *rbm8a*-perturbed zebrafish embryos feature a mild, yet functionally significant attenuation of non-canonical Wnt/PCP signaling involved in convergence and extension movements and other cell polarity coordination. Defective PCP signaling could impact the proper migration, and subsequently influence the cell fate determination of, the LPM stripes and the hematopoietic/endothelial progenitors.

Zebrafish Rbm8a deficiency causes aberrant LPM morphology

As the phenotypes in TAR Syndrome arise in LPM-derived organs and cell types, we next sought to determine if the early LPM develops normally upon *rbm8a* perturbation. To observe LPM formation and patterning after gastrulation, we performed light sheet-based live imaging using the transgenic reporter *scl:EGFP* that marks the emerging hematopoietic and endothelial progenitors in the medial LPM from early somitogenesis stages (**Fig. 4A)** (Davidson and Zon, 2004; Dooley et al., 2005; Zhang and Rodaway, 2007).

In wildtype, the bilateral *scl*-expressing LPM stripes gradually widen and thicken before starting an anterior-to-posterior midline migration around the 5 somite-stage (**Fig. 4B,E,F**). In contrast, *rbm8a* knockdown with *MO-rbm8aATG* resulted in reduced area and volume of the *scl:EGFP*-expressing LPM in the same developmental time span (**Fig. 4C,E,F**). At the imaging endpoint at 10-11 somites, EGFP fluorescence from *scl:EGFP* showed no discernible difference in intensity between wildtype and morphants, yet their overall morphology in mutants appeared wider apart and less converged to the midline (**Fig. 4B,C,E,F**). This reduced convergence is unlikely due to developmental delay, as we stage-matched the analyzed embryos by morphology and not absolute time post-fertilization.

Reflective of the central role of Vangl2 in relaying PCP signaling (Love et al., 2018; Roszko et al., 2015; Yang and Mlodzik, 2015), zebrafish embryos mutant for *vangl2* and morphants show severe convergence and extension defects, resulting in embryos with shortened, wider posterior trunks and compacted tails (Hammerschmidt et al., 1996; Jessen et al., 2002; Li et al., 2013; Marlow et al., 1998; Prince and Jessen, 2019; Roszko et al., 2015; Solnica-Krezel et al., 1996; Whitfield et al., 1996). Consistent with these defects, *vangl2* MO knockdown resulted in reduced volume and width of the *scl:EGFP*-expressing LPM stripes with no discernible impact on fluorescent reporter levels (**Fig. 4D-F, Supplemental Table 8**). Together, these observations indicate that the *scl*-expressing LPM in both *rbm8a*- and in *vangl2*-perturbed embryos develops an aberrant morphology.

***rbm8a*-mutant embryos show convergence and extension defects**

Non-canonical Wnt/PCP signaling controls cell migration during convergence and extension movements that drive zebrafish embryonic axis elongation (Hammerschmidt et al., 1996; Heisenberg et al., 2000; Jussila et al., 2022; Love et al., 2018; Whitfield et al., 1996; Yang and Mlodzik, 2015). Hallmarks of defective convergence and

extension include reduced length of the anteroposterior axis and increased width of the neural plate and somites (Hammerschmidt et al., 1996; Heisenberg et al., 2000; Jessen et al., 2002; Kilian et al., 2003; Marlow et al., 2002; Pierpont et al., 2018; Solnica-Krezel et al., 1996; Topczewski et al., 2001; Williams and Solnica-Krezel, 2020). To document and quantify if *rbm8a* perturbation causes convergence and extension defects in zebrafish, we measured morphometric parameters during early somite stages of wildtype and *rbm8a*-mutant embryos: measured parameters included axis length, somite and neural plate width, three morphometric parameters affected by reduced convergence and extension in PCP mutants. To assign landmarks for these measurements, we combined *in situ* hybridization for *dlx3b*, *tbxta*, *myoD*, and *hgg1* as markers of the neural plate border, chordamesoderm, somites, and prechordal plate, respectively (Akimenko et al., 1994; Schulte-Merker et al., 1994a; Schulte-Merker et al., 1994b; Vogel and Gerster, 1997; Weinberg et al., 1996).

Compared to stage-matched wildtype siblings *rbm8a*$^{\Delta 5/\Delta 5}$ mutants showed significantly reduced axis lengths at the analyzed 6-13 somite stages (**Fig. 5A,B, Supplemental Table 9**). The axis length discrepancy was already detectable at the first developmental time point we measured: while mutant embryos continued to extend in length, they fell short of reaching wildtype lengths at the end of our stage series (**Fig. 5A,B, Supplemental Table 9**). Compared to wildtype, *rbm8a* mutants also featured wider somites and neural plates throughout the analyzed time course (**Fig. 5A,C,D, Supplemental Table 9**).

While milder than phenotypes observed in mutants for core regulators of the process such as *kny* or *vangl2* (Hammerschmidt et al., 1996; Topczewski et al., 2001), these results indicate that somite-stage *rbm8a*-mutant zebrafish embryos show phenotypes consistent with convergence and extension defects.

Non-canonical Wnt/PCP signaling is sensitive to Rbm8a levels

We next tested whether non-canonical Wnt/PCP signaling is sensitive to attenuated Rbm8a levels. We used previously established morpholino oligonucleotides to reduce the levels of the intron-retained PCP ligands, *wnt5b* and *wnt11f2*, as well as transmembrane PCP core components *fzd7a* and *vangl2*: each morpholino has a well-established injection dose that recapitulates the recessive mutant phenotypes of each respective gene as previously validated per current guidelines (Merks et al., 2018; Mosimann et al., 2015; Panakova et al., 2010; Stainier et al., 2017).

To determine whether reduction of non-canonical PCP core components sensitizes zebrafish embryos to reduced Rbm8a levels, we co-injected *MO-rbm8aATG* (**Fig. 6A,B**) together with each PCP core component-targeting morpholino at sub-threshold concentrations into wildtype embryos **(Fig. 6C-F**). We used morphology of the body axis as a read-out to score the level of interaction between *rbm8a* and PCP core components at 48 hpf. Combined knockdown of individual PCP core component genes and *rbm8a* resulted in phenotypes that approached the full-dose knockdown of each Wnt/PCP gene (**Fig 6C-F**). For *fzd7a*, *vangl2*, and *wnt11f2*, over 90% of all co-injected embryos became phenotypic, indicating a strong genetic interaction with *rbm8a* resulting in a predominant severe phenotype class and lower number of moderate phenotypic embryos (**Fig. 6G,**

Supplemental Table 10). *wnt5b* attenuation showed the mildest, yet still significant, response to *rbm8a* co-attenuation with 40% embryos becoming phenotypic (**Fig. 6E,G**). The combined attenuation resulted in embryos with shortened body axes and concomitant circulation defects, as common to perturbations of PCP signaling that affects embryo elongation by convergence and extension (Butler and Wallingford, 2017; Hammerschmidt et al., 1996; Heisenberg et al., 2000; Solnica-Krezel et al., 1996; Whitfield et al., 1996; Williams and Solnica-Krezel, 2020).

To deduce if reducing PCP signaling has a downstream impact on thrombocyte formation, we revisited our *cd41:EGFP*-based thrombocyte counts (**Fig. 2**). We injected cohorts of *cd41:EGFP* embryos with two sub-optimal doses of morpholinos against *vangl2* and *wnt5b*, respectively; injection of each resulted in viable larvae with shortened body axis while establishing seemingly normal blood circulation in the observed timeframe (**Fig. 6H-K**). Compared to control morpholino-injected animals, both *vangl2*- and *wnt5b*-attenuated zebrafish harbored reduced numbers of *cd41:EGFP*-expressing thrombocytes with a clear dose response at 6 dpf (**Fig. 6K, Supplemental Table 2**).

Taken together, our injection-based genetic interaction series established that reduced levels of *rbm8a* sensitize zebrafish embryos to perturbations in components of the non-canonical Wnt/PCP pathway during early development, with consequences to later stages. These observations connect with our morphometric data (**Fig. 4,5**), indicating that *rbm8a*-mutant zebrafish show features of defective convergence and extension that also affect the hematopoietic progenitors among the LPM.

Perturbing *rbm8a* or *vangl2* impacts hematopoietic gene expression

Following bilateral stripe emergence, *scl:EGFP*-positive cells in the converging *drl:mCherry*-positive LPM form hematopoietic, and endothelial fates in the trunk (**Fig. 7A**) (Prummel et al., 2020; Zhang and Rodaway, 2007). We therefore sought to evaluate possible changes to hematopoietic and endothelial progenitor formation and patterning upon *rbm8a* and *vangl2* perturbation, respectively. If attenuation of *rbm8a* results in PCP signaling defects that subsequently cause LPM migration and hematopoietic fate disruptions, we would also anticipate that interrupted PCP signaling in *vangl2* mutants reveals comparable phenotypes. We performed mRNA *in situ* hybridization (ISH) on *rbm8a*$^{\Delta5/\Delta5}$, *rbm8a*$^{\Delta3/\Delta3}$, *MO-rbm8aATG*-injected, *vangl2*$^{vu67/vu67}$, and wildtype control embryos with a panel of marker genes expressed in in hematopoietic and endothelial progenitors (*sox7*, *gata1*, *gfi1aa*, *runx1*, *kdrl*, and *gfi1b*) (**Fig. 7B-F, Supplemental Fig. 4**). *In situ* hybridization for the pan-trunk muscle marker *myoD* provided a reference across conditions and for overall embryo morphology (**Fig. 7B**). We stage-matched embryos to wildtype and control *MO*-injected controls by somite number and overall morphology to ensure valid comparisons and quantifications.

Compared to wildtype control and control MO-injected embryos, we observed decreased and patchy expression of the early pan-endothelial cell markers *sox7* (**Fig. 7C**) and *kdrl* (**Supplemental Fig. 4A**) in the trunk of *rbm8a*$^{\Delta5/\Delta5}$ genotyped embryos (n=2/2 *sox7* (total n=14/48), n=2/8 *kdrl* (total n=22/93)), as well as in *MO*-

rbm8aATG-injected embryos (n=12/23 *sox7*, n=10/55 *kdrl*) (Charney et al., 2017; Davidson and Zon, 2004; Herpers et al., 2008). In comparison, the anterior endothelium and endocardial progenitor fields showed variable reduction of *sox7* and *kdrl* expression in *MO-rbm8aATG*-injected embryos (**Fig. 7C, Supplemental Fig. 4A**). While still expressing *sox7* and *kdrl* at overall comparable levels to wildtype siblings, *vangl2*$^{vu76/vu67}$ embryos (n=6/12 *sox7*, n=2/10 *kdrl*) showed no discernible midline fusion of the bilateral *kdrl*-expressing progenitors in the trunk at 18 somite stage (ss), in line with perturbed convergence and extension and midline migration **(Fig. 7C, Supplemental Fig. 4A**).

The erythroid progenitor marker *gata1* at 18 ss reveals the emerging primitive red blood cells in the intermediate cell mass of the trunk (**Fig. 7A,D**) (Davidson and Zon, 2004; Long et al., 1997). In both stage-matched, genotyped *rbm8a*$^{\Delta5/\Delta5}$ (n=6/11 (total 47/68)) and *MO-rbm8aATG*-injected embryos (n=32/57), *gata1* expression was reduced or patchy compared to wildtype embryos by visual inspection and *in situ hybridization* signal quantification (wildtype n=25, *MO-rbm8aATG*-injected n=24; $p < 0.0001$, using Mann Whitney test) (**Fig. 7D,G, Supplemental Table 11**). Similarly, *gata1* expression in *vangl2*$^{vu76/vu67}$ embryos remained in the posterior-most LPM, yet was greatly reduced in the trunk (n=7/17) (**Fig. 7D**).

The transcription factors GFI1 and GFI1B are key determinants of myeloid fate potential towards erythroid/megakaryocyte and lymphoid fates in mammals, and mutations in human *GFI1B* cause thrombocyte deficiencies (Beauchemin and Möröy, 2020). In zebrafish, the orthologs *gfi1aa* and *gfi1b* influence primitive erythroid precursor formation and are expressed in intermediate and definitive precursors (**Fig. 7A**) (Cooney et al., 2013; Moore et al., 2018; Wei et al., 2008). Compared to wildtype, both genotyped *rbm8a*$^{\Delta5/\Delta5}$ (n=4/6, total 27/41) and *MO-rbm8aATG*-injected embryos (n=12/20) displayed reduced *gfi1aa* expression, which we verified by signal intensity comparison (wildtype n=23, *MO-rbm8aATG*-injected n=21; p=0.0310, using Mann-Whitney test). (**Fig. 7E,G**). *gfi1aa* expression was also markedly reduced in *vangl2*$^{vu76/vu67}$ embryos compared to wildtype siblings (n=16/27; absent quantification due to the deformed yolk masking most of the signal). In contrast, *gfi1b* expression showed no quantitative differences (wildtype n=10, *MO-rbm8aATG*-injected n=23; p=0.0526, using Mann-Whitney test), yet we observed individual *rbm8a*$^{\Delta5/\Delta5}$ embryos with patchy *gfi1b* expression (genotyped n=3/6 (total 14/45))(**Fig. 7G, Supplemental Fig. 4B**).

Lastly, *runx1* expression that marks prospective hematopoietic stem cell progenitors in the trunk (**Fig. 7A**) (Kalev-Zylinska et al., 2002) was reduced upon *rbm8a* perturbation at 18 ss (genotyped *rbm8a*$^{\Delta5/\Delta5}$ n=16/19 mutants, *MO-rbm8aATG*-injected n=26/27) (**Fig. 7F, Supplemental Fig. 4C** for quantification details). Notably, the spinal cord neurons and other domains expressing *runx1* seemed unaffected in number and expression level, a hallmark of mutants with selective hematopoietic defects (**Fig. 7F,J, Supplemental Table 11**) (Horsfield et al., 2007). Although, *vangl2*$^{vu67/vu67}$ embryos maintained *runx1* expression in the eye, ear, and dorsal spinal cord neurons, they displayed selectively reduced or absent *runx1* expression in the presumptive hematopoietic stem cell progenitors at the midline as well as posterior blood island (PBI) (n=6/8) (**Fig. 7F,H**,**I, Supplemental Table 11**). Notably, this impaired *runx1* expression in both *rbm8a*$^{\Delta5/\Delta5}$ and *vangl2*$^{vu76/vu67}$ embryos is unlikely to

be caused by developmental delay or the severely perturbed midline migration in *vangl2*$^{vu76/vu67}$ embryos, as *runx1* expression is stronger in earlier bilateral LPM progenitors before confining to hematopoietic stem cell precursors (**Fig. 7A,F**) (Horsfield et al., 2007; Kalev-Zylinska et al., 2002).

While only including a limited sampling of perturbations and timepoints, together these data document select changes in hematopoietic progenitor gene expression upon *rbm8a* and *vangl2* defects. Our data proposes a model in which attenuated Rbm8a levels and concomitant EJC reduction result in retention of mis-spliced mRNAs encoding non-canonical Wnt/PCP genes (among others), lowering the effective protein concentration of several PCP pathway components; this results in sub-optimal convergence and extension and cell migration including LPM progenitors, with subsequent impact on hematopoietic progenitor numbers and/or gene expression. In line with this model, zygotic *rbm8a*-mutant and -knockdown zebrafish feature select and significant blood and endothelial lineage defects already prior to the onset of heartbeat and circulation.

DISCUSSION

The striking phenotype combination of TAR syndrome – affecting selective blood and limb skeleton features as well as heart, kidney, and craniofacial structures – has remained challenging to consolidate with a unifying disease mechanism. The identification of hypomorphic defects in the ubiquitous EJC factor Rbm8a in TAR syndrome patients has further complicated possible explanations of how the selective phenotypes arise. Investigating the developmental impact following different means of reducing Rbm8a protein levels in zebrafish, we propose that TAR syndrome involves early embryonic perturbations in LPM formation and patterning via attenuated PCP signaling. Our work links sensitizing reduction of pathways essential for embryo morphogenesis to retained introns in individual mRNAs upon Rbm8a reduction, proposing a developmental mechanism to consolidate the seemingly divergent phenotypes of TAR syndrome as LPM-affecting birth defect.

Disruption of a molecular mechanism that is shared in the development of diverse cell fates by means of clonal cell relationship, evolutionary co-option, or signaling interactions between progenitors can lead to complex syndromic phenotypes. Mutations in pleiotropic factors such as ribosomal or DNA repair components have been linked to hematological disorders with additional structural defects that include the limbs as observed in Diamond-Blackfan Anemia and Fanconi's Anemia, respectively (Bhandari et al., 2022; Gazda et al., 2006; Landowski et al., 2013; Parmar et al., 2009; Stoll et al., 2013; Thompson et al., 2001). Curiously, distinct rare congenital cases with combined amegakaryocytic thrombocytopenia and radial-ulnar anomalies have been reported (CTRUS or RUSAT, OMIM # 605432) (Balduini, 2022). Mutations in *HOXA11* have been linked to thrombocytopenia with concurrent proximal fusion of radius and ulna in affected patients (Thompson and Nguyen, 2000), and *Hox* gene mutations are hypothesized to underlie similar phenotypic manifestations in rare cases (Thompson et al., 2001). Individual patients with initial platelet deficiency that improves with age and deficient pronation-supination of the forearm carry mutations in *MECOM1* encoding the transcription factor EVI-1 (Niihori et al., 2015). Both Hoxa11 and Evi-1 have been associated with hematological, forelimb, and other

LPM-linked disorders (Bard-Chapeau et al., 2012; Davis et al., 1995; Horvat-Switzer and Thompson, 2006; Konantz et al., 2016; Li et al., 2022; Mugford et al., 2008; Patterson et al., 2001; Perkins et al., 1991; Yokomizo et al., 2022; Yuan et al., 2015). Independent of underlying molecular mechanism, establishing a developmental connection between affected cell types in syndromic congenital disease provides a potent framework to expand diagnosis, phenotype assessment, and long-term care of affected patients. The multi-lineage potential of early LPM provides a developmental concept to connect seemingly disparate syndromic phenotypes as outlined above and to potentially regard them as LPM diseases (Kocere et al., 2023).

rbm8a perturbation in zebrafish has increasingly pleiotropic defects as described here and in previous work (Gangras et al., 2020), in line with Rbm8a protein function in the ubiquitously deployed EJC that regulates diverse mRNA biology (Chuang et al., 2015; Hir et al., 2015; Le Hir and Andersen, 2008; Palacios et al., 2004). Elegant genetic experiments have documented how the 3' UTR intron-containing *foxo3b* mRNA that encodes a pro-apoptotic transcription factor is stabilized in *rbm8a*-mutant embryos, while double *rbm8a;foxo3b* mutants showed a significant rescue of the motor neuron defects (Gangras et al., 2020). Not surprisingly, recessive null combinations of human RBM8A mutations have never been reported and are likely not viable; all genetically investigated TAR patients reported to date harbor at least one hypomorphic allele of *RBM8A*, suggesting reduced EJC levels or activity result in the combination of syndromic phenotypes (Albers et al., 2012; Boussion et al., 2020; Pang et al., 2020; Petit and Boussion, 2022). The combination of waning maternal contribution, morpholino-based dose attenuation, and our hypomorphic *rbm8a*$^{\Delta 3}$ allele in zebrafish provides *in vivo* means to approximate the assumed hypomorphic reduction of RBM8A levels in human TAR patients. In line with morpholino guidelines (Stainier et al., 2017), *MO-rbm8aATG* injection morphologically phenocopy *rbm8a*$^{\Delta 5/\Delta 5}$, reduces Rbm8a protein levels, is rescued with human RBM8A mRNA while expression lasts, and can be titrated for genetic interactions (**Fig. 1,2,6, Supplemental Fig. 1,2**).

Our observations that different PCP perturbations result in select hematopoietic defects (**Fig. 3,6**) provide a first mechanistic direction to consolidate the TAR defects. Convergence and extension in an embryo influences nearly all tissues and overall body architecture (Hammerschmidt et al., 1996; Jessen et al., 2002; Yamanaka et al., 2007). The LPM undergoes dramatic cellular and structural changes during convergence and extension movements, resulting in condensed bilateral stripes at the periphery of the embryo. The subsequent midline migration of hematopoietic, endothelial, and kidney progenitors is sensitive to perturbations of guidance cues, yet the exact mechanism(s) that trigger and drive midline migration remain incompletely resolved. PCP signaling defects prevent condensation of all germ layers along the anterior-posterior axis, keeping especially the LPM as lateral-most cells widely dispersed (Hammerschmidt et al., 1996; Jessen et al., 2002; Roszko et al., 2009; Whitfield et al., 1996; Xing et al., 2018; Yin and Solnica-Krezel, 2007).

One possible explanation could be that as hematopoietic progenitors migrate as medial-most LPM stripe and are exposed to different signals and cellular interactions during their migration, attenuated PCP could interrupt hematopoietic progenitor arrangement and migration speed. This model is in line with our observations of altered

scl:EGFP-expressing LPM in *rbm8a* and *vangl2* perturbations (**Fig. 4**). However, in both *rbm8a* and *vangl2* mutants hematopoietic progenitors do still form, albeit with altered expression of individual regulatory genes (**Fig. 7**). We therefore hypothesize that, following Rbm8a perturbations, attenuated PCP through retention of mis-spliced mRNAs encoding non-canonical Wnt/PCP components affects migration or relative position of hematopoietic progenitors within the embryo as they migrate through signaling gradients. Notably, mice with defects in the EJC component Srsf3 also display thrombocytopenia (Heazlewood et al., 2022). The progressive recovery of the thrombocytopenia phenotype in TAR patients is compatible with an early defect in embryonic or fetal hematopoiesis when transient or intermediate progenitor waves are forming; the high plasticity and clonal expansion even of potentially reduced hematopoietic stem cells could subsequently replenish the diminished megakaryocyte levels during definitive hematopoiesis (Albers et al., 2013; Bonsi et al., 2009; Doulatov et al., 2012; Orkin and Zon, 2008; Petit and Boussion, 2022; Pinho and Frenette, 2019; Zhang et al., 2018). The reduced *gfi1aa* expression (**Fig. 7**) and later reduced numbers of *cd41:EGFP*-expressing thrombocytes in our quantifications following *rbm8a* and PCP perturbations show signs of compensation over time (**Fig. 2,6**), providing an experimental starting point to pursue this model.

Connecting morphological alterations by attenuating non-canonical Wnt/PCP signaling as major pathway involved in embryo morphogenesis provides a possible mechanistic link to the impact on LPM-derived structures in TAR Syndrome and possibly other congenital conditions. While we here focus on consequences of perturbed *rbm8a* on hematopoiesis, non-canonical Wnt/PCP disruptions have the potential to affect a variety of tissues (Butler and Wallingford, 2017). PCP signaling does not elicit an obvious transcriptional response, confining effects of its perturbation to morphological defects; however, we hypothesize that incorrect or delayed migration or altered arrangement of LPM progenitors could manifest as defects in individual downstream fates by altering the spatio-temporal dynamics of exposure to developmental signals and cell-cell interactions. Such a model would be consistent with recent observations linking emerging cell fates to overall morphogenesis that is a prerequisite for the correct formation of patterning gradients (Fulton et al., 2020). In addition to zebrafish do not forming a radius bone, future work is warranted to decode the basic impact on heart, forelimbs (pectoral fin), kidney, and other LPM-derived structures upon *rbm8a* perturbation. PCP defects have been linked to anomalies in each of these structures in mice (Butler and Wallingford, 2017; Gao and Yang, 2013; Li and Wang, 2018; Li et al., 2016; Li et al., 2019; Merks et al., 2018; Panakova et al., 2010; Sugimura et al., 2012; Wang et al., 2011), further suggesting defective PCP signaling in LPM patterning as corroborating developmental link for the TAR syndrome phenotypes.

METHODS

All research described herein complies with all relevant ethical regulations as reviewed and approved by the University of Colorado Anschutz Medical Campus, the University of Zurich, the MDC Berlin, and Baylor College of Medicine.

Zebrafish husbandry

Zebrafish (*Danio rerio*) husbandry and experiments were performed according to IACUC regulations at the University of Colorado School of Medicine, Anschutz Medical Campus (protocol 00979), FELASA guidelines (Aleström et al., 2020), the guidelines of the Max-Delbrück Center for Molecular Medicine in the Helmholtz association, and the local authority for animal protection (Landesamt für Gesundheit und Soziales, Berlin, Germany). The 'Principles of Laboratory Animal Care' (NIH publication no. 86–23, revised 1985) as well as the current version of German Law on the Protection of Animals and EU directive 2010/63/EU on the protection of animals were followed. All zebrafish were raised, kept, and handled according to established protocols if not noted otherwise (Westerfield, 2007).

Transgenic zebrafish lines

The following established transgenic lines were used in this study: *Tg(scl:EGFP)*^{zf255} (Zhang and Rodaway, 2007), *Tg(cd41:EGFP)* (Lin et al., 2005), and *Tg(RGB)* (Chiavacci et al., 2017) (combined transgene insertions from *Tg(-6.35drl:EGFP)*^{cz3331} (Mosimann et al., 2015), *Tg(lmo2:loxP-dsRED2-loxP-EGFP)*^{rj2} (Wang et al., 2008), and *Tg(myl7-loxP-AmCyan-loxP_ZsVenus)*^{fb2} (Zhou et al., 2011)).

sgRNA template generation, RNP complex assembly and injection

Oligos were obtained from Sigma/Millipore and Life Technologies as standard primers except where otherwise noted. A short guide RNA (sgRNA) template was generated by oligo-based PCR amplification (Bassett et al., 2013) using the sgRNA forward primer containing a *T7* promoter sequence *5'-GAAATTAATACGACTCACTATAGGGAGGCGAAGACTTTCCTAGTTTTAGAGCTAGAAATAGC-3'* and the invariant reverse primer *5'-AAAAGCACCGACTCGGTGCCACTTTTTCAAGTTGATAACGGACTAGCCTTATTTTAACTTGCTATTTCTAGCTCTAAAAC-3'* (PAGE-purified). A primer extension reaction was performed using Phusion DNA polymerase (M0530L, NEB) followed by QIAquick purification (28106, Qiagen) with elution of the PCR product in DEPC-treated water. *In vitro* transcription (IVT) of the sgRNA-based PCR template was performed using the MAXIscript T7 Kit (AM132, Ambion) with an overnight reaction run at 37°C, followed by ammonium acetate precipitation or clean up via RNA isolation kits as per the manufacturer's instructions and as described previously (Bassett et al., 2013; Gagnon et al., 2014). The only change to the manufacturer's protocol of the MAXIscript T7 Kit was to add 100mM NTPs instead of the recommended 10 mM as this greatly increases sgRNA yield. Before use, the sgRNA was quality controlled on a denaturing 2.5% MOPS gel. The CRISPR-Cas9 ribonucleoprotein complex (RNPs) was assembled using appropriate salt concentrations to keep the RNPs solubilized (Burger et al., 2016). Salt-solubilized RNPs were then injected at sub-optimal concentrations to increase viability and founder identification (Burger et al., 2016).

Mutant zebrafish lines

rbm8a mutant alleles were generated as per our previous work (Burger et al., 2016) using the target site 5'-*GGGAGGCGAAGACTTTCCTA-5'* as proposed by CHOPCHOP (Montague et al., 2014). Details about sgRNA template generation and RNP complex assembly and injection are described in the Supplemental Data. The two

alleles *rbm8a*$^{\Delta 5}$ (also described in Gangras et al., 2020) and *rbm8a*$^{\Delta 3}$ were selected. Both alleles were genotyped by sequencing PCR products using primer *rbm8a fwd 5'-AAACAGCAGACGGCGAGG-3'* and primer *rbm8a rev 5'-GCTGAATCACTACAACGCG-3*'. Additionally, the *rbm8a* wildtype allele was genotyped by restriction digest of the PCR product with Xmn1 (R0194S, NEB) and the *rbm8a*$^{\Delta 3}$ allele by Hinf1 (R0155S, NEB) while the *rbm8a*$^{\Delta 5}$ allele stayed intact upon Xmn1 or Hinf1 digest.

Further, the established *vangl2*^{vu67} mutant was used (Li et al., 2013) (a kind gift from Dr. Liliana Solnica-Krezel). Embryos were genotyped by sequencing PCR products using primer *vangl2 fwd 5'-ATTCCCTGGAGCCCTGCGGGAC-3'* and primer *vangl2 rev 5'-AGCGCGTCCACCAGCGACACAGC-3*' or restriction digest of the PCR products with Alu1 (R0137S, NEB). The *vangl2* wildtype allele stayed intact while the *vangl2*^{vu67} mutant allele was identified by a digested PCR product.

Morpholino injections and rescue experiments with capped mRNA

Capped mRNA for mutant rescue was generated using the mMESSAGE mMACHINE™ SP6 Transcription Kit (AM1340, Ambion) as per the manufacturer's instructions. As templates, *pCS2+:EGFP* (Turner and Weintraub, 1994) and *pCS2FA:hs_RBM8A* were used. To generate the original *pCS2FA:hs_RBM8A*, the human *RBM8A* ORF was amplified from HEK293T cDNA by PCR with primer *fwd 5'-TTAGGATCCATGGCGGACGTGCTAGATC-3'* containing a *BamHI* site (underlined) and primer *rev 5'-TTGCTAGCTCAGCGACGTCTCCGGTCT-3'* containing a *NheI* site (underlined). The PCR product was cloned with BamHI (R0136S, NEB), NheI (R3131S, NEB) restriction digest into Tol2kit vector *396* (*pCS2FA:Tol2*) (Kwan et al., 2007) cut with BamHI and XbaI (R0145S, NEB).

Morpholinos were obtained from Gene Tools (Philomath, USA) and prepared as a 1 mM stock solution according to the manufacturer's instructions. To target *rbm8a*, a translation blocking morpholino, *MO-rbm8aATG* with sequence *5'-GAAGATCCAGTACGTCCGCCATGA-3'* (sequence complementary to predicted start codon is underlined), was designed and diluted as indicated. All other morpholinos used in this study have been published previously and morpholino details and injection procedures are described in the Supplemental Data.

Rescue experiments were performed by injecting *MO-rbm8aATG* (1:100 dilution) and 100 ng/µL capped *hs_RBM8A(altered)* mRNA and *EGFP* mRNA as control. As the codons encoding the N-terminus of zebrafish and human RBM8A protein are identical in the respective mRNAs and therefore also human *RBM8A* mRNA is recognized by the *MO-rbm8aATG*, 5' codons in the morpholino-targeted region were altered to synonymous codons where possible: wildtype human *RBM8A 5'-ATGGCGGACGTGCTAGATCTTCACGAGGCTGGG-3'* to *5'-atggcAgaTgtCTtGgaCTtGCAC-3'* (alterations in capital letters, resulting in synonymous codons, *ATG* start codon underlined in both sequences). The resulting *RBM8A(altered)* ORF was ordered from Twist Biosciences and swapped into *pCS2FA:hs_RBM8A* with flanking BamHI and NheI sites as above, resulting in *pCS2FA:hs_RBM8A(altered).* mRNA was generated and injected as outlined above.

The embryos were observed for phenotypes at 24, 48 and 72 hpf and representative images were taken with a 10x lens on a Zeiss LSM880. Observed phenotypes were plotted in percent using GraphPad Prism (v9.3.0.).

Additional morpholinos and injection procedures

MO1-vangl2 (ZFIN ID: *ZDB-MRPHLNO-041217-5*, 5'-*GTACTGCGACTCGTTATCCATGTC*-3'), *MO2-wnt5b* (ZFIN ID: *ZDB-MRPHLNO-051207-1*, *5'-TGTTTATTTCCTCACCATTCTTCCG-3'*) , *MO2-wnt11f2* (formerly known as *MO2-wnt11* or *wnt11-MO*, ZFIN ID: *ZDB-MRPHLNO-050318-3*, 5'-*GTTCCTGTATTCTGTCATGTCGCTC*-3') and *MO1-fzd7a* (ZFIN ID: ZDB-*MRPHLNO-050923-5*, *5'-ATAAACCAACAAAAACCTCCTCGTC-3'*) which we have described previously and validated (Fong et al., 2005; Kim et al., 2005; Matsui et al., 2005; Merks et al., 2018; Stainier et al., 2017; Takamiya and Campos-Ortega, 2006), have been used at indicated dilution. Lastly, the Gene Tools pre-made standard control oligo morpholino (100 nmol) was used.

Prior to injections, the 1mM morpholino stock solution was heated up to 65°C, vortexed for 5 minutes and diluted to achieve the desired concentrations. The diluted morpholino solution was again heated to 65°C and vortexed for 10 minutes before injecting. All morpholino solutions were stored at room temperature.

Microinjections were performed using MPPI-3 microinjectors (Applied Scientific Instrumentation) together with a Narishige micromanipulator (MN-153). Morpholino oligonucleotides were injected into the yolk of one-cell stage zebrafish embryos. The injection volume was calibrated to the final volume of 1 nL in total. In case of double knockdown approaches to study genetic interactions, both morpholinos were injected sequentially. Embryos were kept in E3 embryo medium under standard laboratory conditions at 28.5°C.

Zebrafish protein sample collection

Zebrafish embryos were collected at indicated developmental stages (tailbud stage, 10 somite stage, 16 somite stage, 24 hpf). Individual embryos were transferred into tubes kept on ice filled with 200 µL cell dissociation solution (CDS; 5 ml of Ringers' solution (96724, Sigma), 1 tablet of Complete Mini EDTA-free (11836153001, Roche). The embryos in CDS were flash frozen in liquid nitrogen and samples were stored at -80°C until they were genotyped and could be combined according to their genotype for further usage. For genotyping, a few cells from individual embryos were collected and genotyped as described above.

After combining 10 embryos with the same genotype for each developmental stage, the samples were centrifuged at 1500 rpm for 2 minutes at 4°C. The tubes were turned by 180° and centrifuged for 2 additional minutes. The supernatant was removed, 200 µL CDS was added, and centrifuged again as above. Afterwards, the supernatant was again removed, and the samples centrifuged once more with additional removal of the remaining supernatant using fine gel loading tips. Then, 20 µL 2x SDS Laemmli buffer (1610747, BioRad) supplemented with 5% 2-betamercaptaethanol (M3148, Sigma) was added to each sample, vortexed rigorously, and cooked for 5 min at 95 °C.

Electrophoresis and immunoblot analysis

Samples were loaded on a precast Mini-PROTEAN TGX gel (4569034, Biorad) and electrophoresis was performed as per the manufacturer's instructions. Afterwards, the gel was transferred onto a PVDF membrane (1704272, Biorad) using the trans-blot turbo transfer system (1704150, Biorad).

Zebrafish Rbm8a and Tubulin proteins were detected using standard immunodetection protocols, in short: blocking with 1XTTBS 5% BSA for 1 hour, overnight incubation with anti-Rbm8a (1:1000; 05-1511, Millipore),

anti-Tubulin (1:1000; 05-829, Millipore) in 1XTTBS 5% BSA at 4 °C, followed by 3 x 5 min wash in TTBS and 30 min incubation with IRDye 800CW goat anti-Mouse (1:10000; 926-32210, Li-Cor) in 1XTTBS 5% BSA at room temperature followed by 3 x 5 min wash in 1XTTBS. Images of Western blots were obtained using an Odyssey CLx imager (Li-Cor) and quantified using ImageJ (https://www.yorku.ca/yisheng/Internal/Protocols/ImageJ.pdf). All full gel images are shown Supplemental Figure 1.

cd41:EGFP-positive cell counting

For live imaging of 3 and 6 dpf *cd41:EGFP* zebrafish larvae, the heartbeat was stopped with 30 mM 2,3-butanedione monoxime (BDM; B0753, Sigma) in E3, in addition to anesthesia with Tricaine. Images of the zebrafish larvae used for thrombocyte counting were taken on a Leica M205 FA with Plan Apo 1.0x lens. 3 dpf larvae were imaged directly in E3+BDM+Tricaine on a glass plate, while the 6 dpf larvae were placed on a petri dish covered with a 2% agarose layer. Larvae were placed anterior to the left. The images were taken consistently at 2x zoom for groups of three zebrafish for 3 d pf and 3x zoom for single zebrafish at 6 dpf. For analysis, the images are exported from LAS Leica, and using Fiji/ImageJ macro (Schindelin et al., 2012), the GFP channels are separated. Next, for 3 dpf, the cells were counted manually by adjusting brightness and contrast as needed, using the Fiji/ImageJ cell counter plugin (https://imagej.nih.gov/ij/plugins/cell-counter.html). For 6 dpf, a second Fiji/ImageJ macro was run that thresholds and automatically counts the cells. Individual data points, means, and ± S.D. were plotted using GraphPad Prism (9.3.0.). Representative images of 6 dpf larvae for figure panels were taken on a Zeiss LSM880 with 10x lens.

Macros to run on imaging files in an individual folder:

```
##Macro 1##
          // ask user to select a folder
          dir = getDirectory("Select a folder");
          // prepare a folder to output the images
          output_dir = dir + File.separator + " output" + File.separator;
          File.makeDirectory(output_dir);
          list = getFileList(dir);
          for (i=0; i<list.length; i++) {
           showProgress(i+1, list.length);
           open(dir+list[i]);
           }
          for (i=0; i<200; i++) {
               imageTitle=getTitle();
          selectWindow(imageTitle);
          run("Split Channels");
          selectWindow("C3-"+ imageTitle);
          close();
```

```
selectWindow("C1-"+ imageTitle);
close();
selectWindow("C2-"+ imageTitle);
run("Subtract Background...", "rolling=10");
saveAs("tiff", output_dir+imageTitle);
close();
}
```

##Macro 2##

```
// ask user to select a folder
dir = getDirectory("Select A folder");
list = getFileList(dir);
for (i=0; i<list.length; i++) {
 showProgress(i+1, list.length);
 open(dir+list[i]);
 }
for (i=0; i<200; i++) {
      imageTitle=getTitle();
      selectWindow(imageTitle);
      run("16-bit");
      setAutoThreshold("Default dark");
      run("Threshold...");
      waitForUser("done");
      setOption("BlackBackground", false);
      run("Convert to Mask");
      run("Watershed");
      setTool("polygon");
      run("Analyze Particles...", "  show=Outlines display clear
summarize add");
      setTool("hand");
            close();
            close();
}
```

Upon completion, toggle the top bar until all cd41:EGFP-bright cells are covered, press "ok" in dialog window. Resulting data was processed in Excel for next steps.

Bulk RNA sequencing data analysis

RNA sequencing reads were initially quality checked with FastQC (https://www.bioinformatics.babraham.ac.uk/projects/fastqc/) and MultiQC (Ewels et al., 2016) and deemed of high quality. We quantified transcript-level expression using Salmon (version 0.8.2) (Patro et al., 2017) against the Ensembl GRCz10.87 catalog (Aken et al., 2017) and performed gene-level differential expression using tximport (version 1.4.0) (Soneson et al., 2016b) and edgeR (version 3.18.1) (Robinson et al., 2010) using the quasi-likelihood F test (Lun et al., 2016) and a Benjamini-Hochberg multiple testing correction (Benjamini and Hochberg, 1995); thresholds were set at FDR <= 0.05. Volcano plots were produced using the ggplot2 (version 2.2.1) package. RNA-seq reads were also mapped against the GRCz10 reference genome with STAR (version 2.5.1b_modified) (Dobin et al., 2013), using the Ensembl GRCz10.87 catalog. Coverage tracks (in bigWig format) were created with bedtools (version 2.17.0) (Quinlan and Hall, 2010) and bedGraphToBigWig (version 4) (Kent et al., 2010) and plotted with Gviz (version 1.20.0) (Hahne and Ivanek, 2016). Differential exon/intron usage analysis was performed using DEXSeq (version 1.22.0) (Anders et al., 2012). Transcripts contributing less than 5% of the abundance for a given gene in all samples were removed from the gtf file (Soneson et al., 2016a) and a gff file with disjoint exon bins were generated from the remaining transcripts using DEXSeq. Finally, introns (regions of a gene locus not belonging to any annotated transcript) were explicitly added as separate bins in the gff file before quantification and differential exon/intron usage analysis with DEXSeq. To explore the RNA-seq data interactively, we created the R/Shiny-based RNAseq Explorer app (link: http://imlspenticton.uzh.ch:3838/mosimann_p2452/). The app contains tabs for various visualizations and analyses: individual gene expression levels (by typing the gene name), a PCA plot for an overall view of the similarity of gene expression profiles, normalized base-level coverage tracks for individual genes, differential expression results, differential transcript usage results, and gene set enrichment analyses. Code for the app and instructions for its use are available at https://github.com/markrobinsonuzh/rbm8a-rnaseq-explorer, with track data downloadable from https://doi.org/10.5281/zenodo.7680271.

Light sheet sample preparation, microscopy, and image analysis

The Zeiss Z.1 microscope equipped with a Zeiss W Plan-Apochromat 20×/0.5 NA objective was used for all light sheet microscopy. Embryos within the chorion were embedded in 1% LMA in a 50 µL glass capillary.

For the multi-angle imaging data sets, the four individual angles per embryo were manually registered before applying the Fiji Multiview Reconstruction and BigStitcher plugins (Hörl et al., 2019; Schindelin et al., 2012) for fusion and deconvolution of the images. Images and movies were further processed using Fiji/ImageJ and Imaris (9.7) (Prummel et al., 2022).

Morpholino-injected embryos were raised at 28 °C and imaged in the Z.1 from 4 somite stage to 12 somite stage, alongside uninjected *scl*:EGFP controls. In Imaris, the baseline and background were subtracted and surface rendering was performed to automate volume and area determination of the fluorescent signal. Individual data points, means and ± S.D. were plotted using GraphPad Prism (9.3.0.).

Whole mount in situ hybridization

Whole-mount in situ hybridization (WISH) was performed according to the Thisse lab protocol (Thisse and

Thisse, 2008). Zebrafish embryos were fixed overnight in 4% PFA (47608, Sigma) in PBS (EC-A500, Life Sciences), dechorionated, rinsed in PBS and dehydrated into methanol. Samples were then rehydrated into PBT (PBS + Tween (P1379, Sigma), treated with Proteinase K (1:10000) (P8108S, NEB) for 2 min, washed in PBT and postfixed in 4% PFA/ 0.2% glutaraldehyde (G5882, Sigma) in PBS for 20 min at RT. Then the samples were incubated for at least two hours in hybridization solution with 50% formamide (in 0.75 M sodium chloride, 75 mM sodium citrate, 0.1% Tween-20 (P1379, Sigma), 50 mg/mL heparin (H3393, Sigma), and 200 mg/mL tRNA (AM7119, Invitrogen)) at 70°C, then hybridized overnight at 70°C with antisense probes diluted approximately 1 ng/μl in hybridization solution. Samples were washed gradually into 2X SSC buffer (0.3 M sodium chloride, 30 mM sodium citrate or AM9763, Invitrogen), and then gradually from SSC to PBT. Samples were blocked at room temperature for several hours in PBT with 2% goat or sheep serum (S2263, Sigma) and 2 mg/mL bovine serum albumin (BSA, 196941, Fisher), then incubated overnight at 4°C with anti-DIG antibody (11093274910, Roche) at 1:5000 in block. Samples were rinsed extensively in PBT and staining buffer (100 mM Tris-HCl pH 9.5, 50 mM MgCl2, 100 mM NaCl, 0.1% Tween 20, 0.3mg/mL tetramizole hydrochloride (T1512, Sigma) in dH20), prior to staining with BM Purple AP staining solution (62321800, Roche). Staining was stopped by washing embryos in PBT.

Antisense riboprobes for in situ hybridization

The templates for all *in situ* hybridization (ISH) probes were generated by PCR amplification using primers and complementary DNA (cDNA) or linearized plasmids. First-strand cDNA was generated from pooled zebrafish RNA isolated from different developmental stages using SuperScript III first-strand synthesis kit (18080051, Invitrogen). Subsequently, DNA templates for ISH probes were generated using first-strand cDNA as a PCR template and primers as specified for each gene of interest; for *in vitro* transcription (IVT), either the *T7* (*5′-TAATACGACTCACTATAG*-3′) or *T3* (5′-*AATTAACCCTCACTAAAG*-3′) promoter sequence was added to the *5′* ends of the reverse primers. PCR reactions were performed under standard conditions as per manufacturer's protocol using Phusion DNA polymerase.

The following primer or plasmids to generate templates for ISH probes were used: *kdrl* (using *pBS-kdrl* (a kind gift from Dr. Leonard I. Zon), linearized with EcoRI (R0101S, NEB), T7 polymerase for IVT) (Thompson et al., 1998); *sox7* (using primer *fwd 5'-CGACCAAAACTCCCTTCCG-3'* and primer rev *5'-AAAA<u>TAATACGACTCACTATAG</u>GGTTGTTGTAGTAGGCTGC-3'*, T7 polymerase for IVT), *gata1* (using primer f*wd 5'-TGGGAAAGACAGTCCCAGG-3'* and primer *rev 5'-AAAAA<u>TAATACGACTCACTATAG</u>GGCCTTCACACTAGTGTGGG-3'*, T7 polymerase for IVT); *runx1a* (using *pBS-runx1a*, linearized with HindIII (R0104S, NEB), T7 polymerase for IVT) (North et al., 2007) (a kind gift from Dr. Teresa V. Bowman); *gfi1aa* (using primer *fwd 5'-TTATCATCAGCCCCGTTACC-3'* and primer *rev 5'-AAAA<u>TAATACGACTCACTATAG</u>GGAATGGACGGCTTTATGTTGC-3'*, T7 polymerase for IVT) (Thambyrajah et al., 2016); *gfi1b* (using primer *fwd 5'-ACCAACCTCAAACGAGAGC-3'* and primer *rev 5'-AAAA<u>TAATACGACTCACTATAG</u>GGATTGTCCATCAACTTCTGTC-3'*, T7 polymerase for IVT) (Thambyrajah et al., 2016), *myoD* (linearized with BamHI, T7 polymerase for IVT) (Weinberg et al., 1996), *dlx3b* (in pBS, linearized with SalI, T7 polymerase for IVT) (Akimenko et al., 1994), *tbxta* (in pBS-KS, linearized with XhoI, T7

polymerase for IVT) (Schulte-Merker et al., 1994a), and *hgg1* (linearized with EcoRI, T7 polymerase for IVT) (Vogel and Gerster, 1997).

Antisense ISH probes were transcribed from their template overnight at 37°C using either MAXIscript T7 Kit (AM132, Ambion) or MAXIscript T3 Kit (AM1316, Ambion) and digoxigenin (DIG)-labeled NTPs (11277073910, Roche) as per the manufacturer's instructions. The resulting RNA probe was treated with TURBO DNase (AM2238, Invitrogen), precipitated with lithium chloride (9480G, Invitrogen) and EtOH, dried, rehydrated in 10-20 µL DEPC-treated water and stored at -80°C until further use.

DNA extraction from fixed WISH zebrafish embryos for genotyping

Residual PBT was removed from embryos and replaced with 50 µL 300mM NaCl. The sample was incubated for 4 hours at 65°C for reverse crosslinking. Afterwards, NaCl was removed and replenished with 50 µl ELB (50 ml: 500 µL 1M Tris pH 8.0, 2.5 ml 1M KCl, 150 µL Tween-20 (P1379, Sigma), 47 ml water) and 4 µL 10mg/ml Proteinase K (P8108S, NEB). The samples were incubated for 8 hours at 55°C followed by 10 min at 98°C to inactivate the Proteinase K. The samples were centrifuged and stored at -20°C until genotyping procedure (see above).

Image analysis for morphometric measurements: axis length and somite/neural plate width

WISH-stained embryos with *myoD*, *dlx3b*, *tbxta*, and *hgg1* were transferred into a clear flat-bottom dish with methylcellulose and imaged using a Nikon SMZ18 stereomicroscope. After imaging, embryos were transferred back in PBT for storage at 4°C or immediately genotyped as described above.

ImageJ was used to visualize and manipulate images of WISH-stained embryos and measurements were made manually using the line tool (Schindelin et al., 2012; Schneider et al., 2012). All images were blinded using the blind rename Perl script (https://github.com/jimsalterjrs/blindanalysis) prior to analysis to avoid researcher bias. Axis length measurements were made by measuring from the anterior to posterior aspects of the *dlx3b* expression domain in lateral-view images. Somite width was taken from dorsal-view images by measuring the left to the right side of the *myoD* expression domain at the same three somite pairs per embryo. To measure width of the neural plate in whole mount embryos, dorsal-view images were collected of each embryo, and a line was drawn from one side of the *dlx3b* expression domain to the other side at the level of the otic placodes. Means and ± S.D. were plotted using GraphPad Prism (9.3.0.).

Image analysis of hematopoietic markers and quantification of ISH signal

WISH-stained embryos with *kdrl*, *sox7*, *gata1*, *runx1*, *gfi1aa*, and *gfi1b* were transferred into a clear flat-bottom dish with glycerol and imaged using a Leica M205 dissecting scope with TL3000 Ergo base, swan neck lamps, Planapo 1.0x M-series objective, and FLEXACAM C1 camera. Quantification of ISH signal for *gata1, gfi1aa*, and *gfi1b* was done as previously described using ImageJ (Dobrzycki et al., 2018). Briefly, after imaging the WISH-stained embryos with consistent parameters, the images were inverted to negative and converted to 8-bit grayscale. A Region of Interest (ROI) containing the ISH expression signal was drawn manually for each embryo using the Freehand selection tool in ImageJ. To define the background, a second ROI with the same shape and

area was created in an unstained region of the trunk, above the ROI with the signal. A value for each region was determined by measuring the average pixel intensity. The pixel intensity of the ISH signal was determined by subtracting the value of the background region from the value of the stained region. Quantification of AGM, PBI, and neuron territories in *runx1*-stained embryos was done by scoring of signal intensity from 1 to 5, by three independent researchers, and average values are presented in the graph. Individual data points, means and ± S.D. were plotted using GraphPad Prism (9.3.0.).

Data Accessibility

All mRNA sequencing data has been deposited at ArrayExpress with accession E-MTAB-12503. The related GitHub repository (link: https://github.com/markrobinsonuzh/rbm8a-rnaseq-explorer) hosts code and R objects to support the R/Shiny app for exploring *rbm8a* mutant RNA-seq experiments interactively. All primary data from cell counts and quantifications are included in the Supplemental Data File.

Content of the Supplemental Data File (Excel files):

Supplemental Table 1 Rescue Data for Supplemental Fig 2A to G

Supplemental Table 2 cd41 counts raw data for Fig 2J and K and 6

Supplemental Table 3 DGE_results_filtered_budstage for Fig 3B

Supplemental Table 4 DGE_results_filtered_24hpf_for Fig 3C

Supplemental Table 5 Metascape results for Suppl Fig 3A and B

Supplemental Table 6 DEXSeq_results_filtered_differential intron usage for Fig 3

Supplemental Table 7 DEXSeq_results_filtered_differential exon usage for Suppl Fig 3

Supplemental Table 8 SPIM area and volume raw data for Fig 4

Supplemental Table 9 Axis Somite Neural Plate measurements for Fig 5

Supplemental Table 10 MO coinjection and phenotype analysis raw data for Fig 6

Supplemental Table 11 ISH signal intensity for Fig 7

Competing financial interests

The authors declare no competing financial interests.

Acknowledgements

We thank Christine Archer, Molly Waters, Nikki Tsuji, Ainsley Gilbart, and Olivia Gomez at Anschutz Medical Campus and the aquatic facility staff at MDC for expert zebrafish husbandry support, Sibylle Burger and Cassie L. Kemmler for excellent technical assistance, Dr. Robert L. Lalonde for genotyping troubleshooting, Hannah R. Moran for support with quantifying *runx1 in situ* data, Cassie L. Kemmler for technical support, and past and current members of the Mosimann and Burger labs for critical discussions. We are grateful to the following colleagues for kind reagent sharing and input: Dr. Lilianna Solnica-Krezel for sharing *vangl2*^{vu67} zebrafish; Dr. Teresa V. Bowman and Dr. Leonard I Zon for sharing the *pBS-kdrl* and *pBS-runx1* plasmids; Dr. Martin Gering

for critical input on performing *gfi1aa* and *gfi1b in situ* hybridization; Dr. Martin Jinek for input on EJC interactions and the nature of the isolated *rbm8a* alleles; Dr. Guramrit Singh for pointers concerning functional Rbm8a antibody alternatives; Drs. Raghunath Azhwar and Jordan Shavit for input on *cd41:EGFP* quantification. Schematics that include Biorender.com elements are indicated in the corresponding figure legends.

Financial Support

This work has been supported by NIH/NIDDK grant 1R01DK129350-01A1 and an UZH URPP "Translational Cancer Research" seed grant to A.B.; a project grant from the Swiss Cancer League and the SwissBridge Foundation to C.M. and A.B.; a Swiss National Science Foundation (SNSF) professorship (PP00P3_139093) and Sinergia Grant (CRSII5_180345), a Marie Curie Career Integration Grant from the European Commission (CIG PCIG14-GA-2013-631984), the Canton of Zürich, the UZH Foundation for Research in Science and the Humanities, the UZH Science Alumni, Blutspende Zürich, National Science Foundation Grant 2203311, the University of Colorado School of Medicine, and the Children's Hospital Colorado Foundation to C.M.; SNSF grants 310030_175841 and CRSII5_177208 and University of Zurich's Research Priority Program Evolution in Action to M.D.R..; the Helmholtz Association (ERC-RA-0047), DZHK and BMBF (German Center for Cardiovascular Research and German Ministry of Education and Research, respectively, project X31010011000) to D.P.; an Additional Ventures SVRF grant to C.M., A.B., and D.P.; NIH/NIGMS grant R00HD091386 to M.L.K.W..

Author contributions

A.K., E.C., M.S.H., C.M., A.B., zebrafish experiment design and execution, manuscript writing; C.S., M.D.R., bulk RNA sequencing, data analysis, manuscript writing; J.S.M., M.L.K.W. convergence and extension morphometric measurements, data analysis, manuscript writing; K.M.M.A., D.P., PCP and genetic interaction experiment design and execution, data analysis, manuscript writing.

References

Aken, B. L., Achuthan, P., Akanni, W., Amode, M. R., Bernsdorff, F., Bhai, J., Billis, K., Carvalho-Silva, D., Cummins, C., Clapham, P., et al. (2017). Ensembl 2017. *Nucleic Acids Res.* **45**, D635–D642.

Akimenko, M. A., Ekker, M., Wegner, J., Lin, W. and Westerfield, M. (1994). Combinatorial expression of three zebrafish genes related to distal-less: part of a homeobox gene code for the head. *J. Neurosci.* **14**, 3475–3486.

Albers, C. A., Paul, D. S., Schulze, H., Freson, K., Stephens, J. C., Smethurst, P. A., Jolley, J. D., Cvejic, A., Kostadima, M., Bertone, P., et al. (2012). Compound inheritance of a low-frequency regulatory SNP and a rare null mutation in exon-junction complex subunit RBM8A causes TAR syndrome. *Nat. Genet.* **44**, 435–9, S1-2.

Albers, C. A., Newbury-Ecob, R., Ouwehand, W. H. and Ghevaert, C. (2013). New insights into the genetic basis of TAR (thrombocytopenia-absent radii) syndrome. *Curr. Opin. Genet. Dev.* **23**, 316–23.

Aleström, P., D'Angelo, L., Midtlyng, P. J., Schorderet, D. F., Schulte-Merker, S., Sohm, F. and Warner, S. (2020). Zebrafish: Housing and husbandry recommendations. *Lab. Anim.* **54**, 213–224.

Anders, S., Reyes, A. and Huber, W. (2012). Detecting differential usage of exons from RNA-seq data. *Genome Res.* **22**, 2008–2017.

Ashton-Beaucage, D., Udell, C. M., Lavoie, H., Baril, C., Lefrançois, M., Chagnon, P., Gendron, P., Caron-Lizotte, O., Bonneil, É., Thibault, P., et al. (2010). The Exon Junction Complex Controls the Splicing of mapk and Other Long Intron-Containing Transcripts in Drosophila. *Cell* **143**, 251–262.

Balduini, C. L. (2022). The name counts: the case of "congenital amegakaryocytic thrombocytopenia." *Haematologica*.

Bard-Chapeau, E. A., Jeyakani, J., Kok, C. H., Muller, J., Chua, B. Q., Gunaratne, J., Batagov, A., Jenjaroenpun, P., Kuznetsov, V. A., Wei, C. L., et al. (2012). Ecotopic viral integration site 1 (EVI1) regulates multiple cellular processes important for cancer and is a synergistic partner for FOS protein in invasive tumors. *Proc. Natl. Acad. Sci. U. S. A.* **109**, 2168–2173.

Bassett, A. R., Tibbit, C., Ponting, C. P. P. and Liu, J. L. J.-L. (2013). Highly efficient targeted mutagenesis of Drosophila with the CRISPR/Cas9 system. *Cell Rep.* **4**, 220–8.

Beauchemin, H. and Möröy, T. (2020). Multifaceted Actions of GFI1 and GFI1B in Hematopoietic Stem Cell Self-Renewal and Lineage Commitment. *Front. Genet.* **11**, 1268.

Belmonte, R. L., Engbretson, I. L., Kim, J.-H., Cajias, I., Ahn, E.-Y. E. and Stachura, D. L. (2021). son is necessary for proper vertebrate blood development. *PLoS One* **16**, e0247489.

Benjamini, Y. and Hochberg, Y. (1995). Controlling the False Discovery Rate: A Practical and Powerful Approach to Multiple Testing. *J. R. Stat. Soc. Ser. B* **57**, 289–300.

Bertrand, J. Y., Kim, A. D., Teng, S. and Traver, D. (2008). CD41+ cmyb+ precursors colonize the zebrafish pronephros by a novel migration route to initiate adult hematopoiesis. *Development* **135**, 1853–1862.

Bhandari, J., Thada, P. K. and Puckett, Y. (2022). Fanconi Anemia. *StatPearls*.

Bono, F., Ebert, J., Lorentzen, E. and Conti, E. (2006). The Crystal Structure of the Exon Junction Complex Reveals How It Maintains a Stable Grip on mRNA. *Cell* **126**, 713–725.

Bonsi, L., Marchionni, C., Alviano, F., Lanzoni, G., Franchina, M., Costa, R., Grossi, A. and Bagnara, G. P. (2009). Thrombocytopenia with absent radii (TAR) syndrome: from hemopoietic progenitor to mesenchymal stromal cell disease? *Exp Hematol* **37**, 1–7.

Bottillo, I., Castori, M., De Bernardo, C., Fabbri, R., Grammatico, B., Preziosi, N., Scassellati, G. S., Silvestri, E., Spagnuolo, A., Laino, L., et al. (2013). Prenatal diagnosis and post-mortem examination in a fetus with thrombocytopenia-absent radius (TAR) syndrome due to compound heterozygosity for a 1q21.1 microdeletion and a RBM8A hypomorphic allele: a case report. *BMC Res. Notes* **6**, 376.

Boussion, S., Escande, F., Jourdain, A.-S. S., Smol, T., Brunelle, P., Duhamel, C., Alembik, Y., Attié-Bitach, T., Baujat, G., Bazin, A., et al. (2020). TAR syndrome: clinical and molecular characterization of a cohort of 26 patients and description of novel non-coding variants of RBM8A. *Hum. Mutat.* **41**, 1220–

1225.

Burger, A., Lindsay, H., Felker, A., Hess, C., Anders, C., Chiavacci, E., Zaugg, J., Weber, L. M. L. M., Catena, R., Jinek, M., et al. (2016). Maximizing mutagenesis with solubilized CRISPR-Cas9 ribonucleoprotein complexes. *Development* **143**, 2025–37.

Butler, M. T. and Wallingford, J. B. (2017). Planar cell polarity in development and disease. *Nat. Rev. Mol. Cell Biol. 2017 186* **18**, 375–388.

Charney, R. M., Forouzmand, E., Cho, J. S., Cheung, J., Paraiso, K. D., Yasuoka, Y., Takahashi, S., Taira, M., Blitz, I. L., Xie, X., et al. (2017). Foxh1 Occupies cis -Regulatory Modules Prior to Dynamic Transcription Factor Interactions Controlling the Mesendoderm Gene Program. *Dev. Cell* **40**, 595-607.e4.

Chen, M. J., Yokomizo, T., Zeigler, B. M., Dzierzak, E. and Speck, N. A. (2009). Runx1 is required for the endothelial to haematopoietic cell transition but not thereafter. *Nature* **457**, 887–891.

Chiavacci, E., Kirchgeorg, L., Felker, A., Burger, A. and Mosimann, C. (2017). Early frameshift alleles of zebrafish tbx5a that fail to develop the heartstrings phenotype. *Matters* **2017030000**, 103168.

Chuang, T.-W., Lee, K.-M. and Tarn, W.-Y. (2015). Function and pathological implications of exon junction complex factor Y14. *Biomolecules* **5**, 343–55.

Cooney, J. D., Hildick-Smith, G. J., Shafizadeh, E., McBride, P. F., Carroll, K. J., Anderson, H., Shaw, G. C., Tamplin, O. J., Branco, D. S., Dalton, A. J., et al. (2013). Teleost growth factor independence (gfi) genes differentially regulate successive waves of hematopoiesis. *Dev. Biol.* **373**, 431–441.

Davidson, A. J. and Zon, L. I. (2004). The “definitive” (and ’primitive’) guide to zebrafish hematopoiesis. *Oncogene* **23**, 7233–7246.

Davis, A. P., Witte, D. P., Hsieh-Li, H. M., Potter, S. S. and Capecchi, M. R. (1995). Absence of radius and ulna in mice lacking hoxa-11 andhoxd-11. *Nat. 1995 3756534* **375**, 791–795.

Dobin, A., Davis, C. A., Schlesinger, F., Drenkow, J., Zaleski, C., Jha, S., Batut, P., Chaisson, M. and Gingeras, T. R. (2013). STAR: ultrafast universal RNA-seq aligner. *Bioinformatics* **29**, 15–21.

Dobrzycki, T., Krecsmarik, M., Bonkhofer, F., Patient, R. and Monteiro, R. (2018). An optimised pipeline for parallel image-based quantification of gene expression and genotyping after in situ hybridisation. *Biol. Open* **7**,.

Dooley, K. a, Davidson, A. J. and Zon, L. I. (2005). Zebrafish scl functions independently in hematopoietic and endothelial development. *Dev. Biol.* **277**, 522–36.

Doulatov, S., Notta, F., Laurenti, E. and Dick, J. E. (2012). Hematopoiesis: A Human Perspective. *Cell Stem Cell* **10**, 120–136.

Ewels, P., Magnusson, M., Lundin, S. and Käller, M. (2016). MultiQC: summarize analysis results for multiple tools and samples in a single report. *Bioinformatics* **32**, 3047–3048.

Fong, S. H., Emelyanov, A., Teh, C. and Korzh, V. (2005). Wnt signalling mediated by Tbx2b regulates cell migration during formation of the neural plate. *Development* **132**, 3587–3596.

Fribourg, S., Gatfield, D., Izaurralde, E. and Conti, E. (2003). A novel mode of RBD-protein recognition in the Y14–Mago complex. *Nat. Struct. Mol. Biol. 2003 106* **10**, 433–439.

Fulton, T., Trivedi, V., Attardi, A., Anlas, K., Dingare, C., Arias, A. M. and Steventon, B. (2020). Axis

Specification in Zebrafish Is Robust to Cell Mixing and Reveals a Regulation of Pattern Formation by Morphogenesis. *Curr. Biol.* **30**, 2984-2994.e3.

Gagnon, J. A., Valen, E., Thyme, S. B. B., Huang, P., Ahkmetova, L., Pauli, A., Montague, T. G. G., Zimmerman, S., Richter, C., Schier, A. F. F., et al. (2014). Efficient mutagenesis by Cas9 protein-mediated oligonucleotide insertion and large-scale assessment of single-guide RNAs. *PLoS One* **9**, e98186.

Gangras, P., Gallagher, T. L., Parthun, M. A., Yi, Z., Patton, R. D., Tietz, K. T., Deans, N. C., Bundschuh, R., Amacher, S. L. and Singh, G. (2020). Zebrafish rbm8a and magoh mutants reveal EJC developmental functions and new 3′UTR intron-containing NMD targets. *PLOS Genet.* **16**, e1008830.

Gansner, J. M., Leung, A. D., Superdock, M., Blair, M. C., Ammerman, M. B., Durand, E. M., Barut, B., Handin, R. I., Stachura, D. L., Lu, C., et al. (2017). Sorting zebrafish thrombocyte lineage cells with a Cd41 monoclonal antibody enriches hematopoietic stem cell activity. *Blood* blood-2016-12-759993.

Gao, B. and Yang, Y. (2013). Planar Cell Polarity in vertebrate limb morphogenesis. *Curr. Opin. Genet. Dev.* **23**, 438.

Gao, L., Tober, J., Gao, P., Chen, C., Tan, K. and Speck, N. A. (2018). RUNX1 and the endothelial origin of blood. *Exp. Hematol.*

Garcia-Martinez, V. and Schoenwolf, G. C. (1992). Positional control of mesoderm movement and fate during avian gastrulation and neurulation. *Dev. Dyn.* **193**, 249–56.

Gazda, H. T., Grabowska, A., Merida-Long, L. B., Latawiec, E., Schneider, H. E., Lipton, J. M., Vlachos, A., Atsidaftos, E., Ball, S. E., Orfali, K. A., et al. (2006). Ribosomal Protein S24 Gene Is Mutated in Diamond-Blackfan Anemia. *Am. J. Hum. Genet.* **79**, 1110–1118.

Greenhalgh, K. L. (2002). Thrombocytopenia-absent radius syndrome: a clinical genetic study. *J. Med. Genet.* **39**, 876–881.

Hahne, F. and Ivanek, R. (2016). Visualizing genomic data using Gviz and bioconductor. *Methods Mol. Biol.* **1418**, 335–351.

Hammerschmidt, M., Pelegri, F., Mullins, M. C., Kane, D. A., Brand, M., van Eeden, F. J., Furutani-Seiki, M., Granato, M., Haffter, P., Heisenberg, C. P., et al. (1996). Mutations affecting morphogenesis during gastrulation and tail formation in the zebrafish, Danio rerio. *Development* **123**, 143–51.

Heazlewood, S. Y., Ahmad, T., Mohenska, M., Guo, B. B., Gangatirkar, P., Josefsson, E. C., Ellis, S. L., Ratnadiwakara, M., Cao, H., Cao, B., et al. (2022). The RNA-binding protein SRSF3 has an essential role in megakaryocyte maturation and platelet production. *Blood* **139**, 1359–1373.

Heisenberg, C. P., Tada, M., Rauch, G. J., Saúde, L., Concha, M. L., Geisler, R., Stemple, D. L., Smith, J. C. and Wilson, S. W. (2000). Silberblick/Wnt11 mediates convergent extension movements during zebrafish gastrulation. *Nature* **405**, 76–81.

Herpers, R., Van De Kamp, E., Duckers, H. J. and Schulte-Merker, S. (2008). Redundant roles for sox7 and sox18 in arteriovenous specification in Zebrafish. *Circ. Res.* **102**, 12–15.

Hir, H. Le, Saulière, J. and Wang, Z. (2015). The exon junction complex as a node of post-transcriptional networks. *Nat. Rev. Mol. Cell Biol. 2015 171* **17**, 41–54.

Hörl, D., Rojas Rusak, F., Preusser, F., Tillberg, P., Randel, N., Chhetri, R. K., Cardona, A., Keller, P. J., Harz, H., Leonhardt, H., et al. (2019). BigStitcher: reconstructing high-resolution image datasets of cleared and expanded samples. *Nat. Methods* **16**, 870–874.

Horsfield, J. A., Anagnostou, S. H., Hu, J. K. H., Cho, K. H. Y., Geisler, R., Lieschke, G., Crosier, K. E. and Crosier, P. S. (2007). Cohesin-dependent regulation of Runx genes. *Development* **134**, 2639–2649.

Horvat-Switzer, R. D. and Thompson, A. A. (2006). HOXA11 mutation in amegakaryocytic thrombocytopenia with radio-ulnar synostosis syndrome inhibits megakaryocytic differentiation in vitro. *Blood Cells. Mol. Dis.* **37**, 55–63.

Jessen, J. R., Topczewski, J., Bingham, S., Sepich, D. S., Marlow, F., Chandrasekhar, A. and Solnica-Krezel, L. (2002). Zebrafish trilobite identifies new roles for Strabismus in gastrulation and neuronal movements. *Nat. Cell Biol.* **4**, 610–615.

Joshi, B., Gaur, H., Hui, S. P. and Patra, C. (2022). Celsr family genes are dynamically expressed in embryonic and juvenile zebrafish. *Dev. Neurobiol.* **82**, 192–213.

Jussila, M., Boswell, C. W., Griffiths, N. W., Pumputis, P. G. and Ciruna, B. (2022). Live imaging and conditional disruption of native PCP activity using endogenously tagged zebrafish sfGFP-Vangl2. *Nat. Commun. 2022 131* **13**, 1–13.

Kalev-Zylinska, M. L., Horsfield, J. A., Flores, M. V. C., Postlethwait, J. H., Vitas, M. R., Baas, A. M., Crosier, P. S. and Crosier, K. E. (2002). Runx1 is required for zebrafish blood and vessel development and expression of a human RUNX1-CBF2T1 transgene advances a model for studies of leukemogenesis. *Development* **129**, 2015–2030.

Kent, W. J., Zweig, A. S., Barber, G., Hinrichs, A. S. and Karolchik, D. (2010). BigWig and BigBed: enabling browsing of large distributed datasets. *Bioinformatics* **26**, 2204.

Kilian, B., Mansukoski, H., Barbosa, F. C., Ulrich, F., Tada, M. and Heisenberg, C. P. (2003). The role of Ppt/Wnt5 in regulating cell shape and movement during zebrafish gastrulation. *Mech. Dev.* **120**, 467–476.

Kim, H. J., Schleiffarth, J. R., Jessurun, J., Sumanas, S., Petryk, A., Lin, S. and Ekker, S. C. (2005). Wnt5 signaling in vertebrate pancreas development. *BMC Biol.* **3**, 23.

Kissa, K. and Herbomel, P. (2010). Blood stem cells emerge from aortic endothelium by a novel type of cell transition. *Nature* **464**, 112–115.

Klopocki, E., Schulze, H., Strauss, G., Ott, C.-E. E., Hall, J., Trotier, F., Fleischhauer, S., Greenhalgh, L., Newbury-Ecob, R. A., Neumann, L. M., et al. (2007). Complex inheritance pattern resembling autosomal recessive inheritance involving a microdeletion in thrombocytopenia-absent radius syndrome. *Am J Hum Genet* **80**, 232–240.

Kocere, A., Lalonde, R. L., Mosimann, C. and Burger, A. (2023). Lateral thinking in syndromic congenital cardiovascular disease. *Dis Model Mech* **16**,.

Konantz, M., Alghisi, E., Müller, J. S., Lenard, A., Esain, V., Carroll, K. J., Kanz, L., North, T. E., Lengerke, C., Adamo, L., et al. (2016). Evi1 regulates Notch activation to induce zebrafish hematopoietic stem cell emergence. *EMBO J.* **459**, 1131–1135.

Kurosaki, T., Popp, M. W. and Maquat, L. E. (2019). Quality and quantity control of gene expression by

nonsense-mediated mRNA decay. *Nat. Rev. Mol. Cell Biol. 2019 207* **20**, 406–420.

Kwan, K. M., Fujimoto, E., Grabher, C., Mangum, B. D., Hardy, M. E., Campbell, D. S., Parant, J. M., Yost, H. J., Kanki, J. P. and Chien, C. Bin (2007). The Tol2kit: a multisite gateway-based construction kit for Tol2 transposon transgenesis constructs. *Dev Dyn* **236**, 3088–3099.

Landowski, M., O'Donohue, M. F., Buros, C., Ghazvinian, R., Montel-Lehry, N., Vlachos, A., Sieff, C. A., Newburger, P. E., Niewiadomska, E., Matysiak, M., et al. (2013). Novel deletion of RPL15 identified by array-comparative genomic hybridization in Diamond-Blackfan anemia. *Hum. Genet.* **132**, 1265–1274.

Le Hir, H. and Andersen, G. R. (2008). Structural insights into the exon junction complex. *Curr. Opin. Struct. Biol.* **18**, 112–119.

Li, D. and Wang, J. (2018). Planar cell polarity signaling in mammalian cardiac morphogenesis. *Pediatr. Cardiol.* **39**, 1052.

Li, X., Roszko, I., Sepich, D. S., Ni, M., Hamm, H. E., Marlow, F. L. and Solnica-Krezel, L. (2013). Gpr125 modulates Dishevelled distribution and planar cell polarity signaling. *Dev.* **140**, 3028–3039.

Li, D., Sinha, T., Ajima, R., Seo, H.-S., Yamaguchi, T. and Wang, J. (2016). Spatial regulation of cell cohesion by Wnt5a during second heart field progenitor deployment. *Dev. Biol.*

Li, D., Angermeier, A. and Wang, J. (2019). Planar cell polarity signaling regulates polarized second heart field morphogenesis to promote both arterial and venous pole septation. *Dev.* **146**,.

Li, J., Glover, J. D., Zhang, H., Peng, M., Tan, J., Mallick, C. B., Hou, D., Yang, Y., Wu, S., Liu, Y., et al. (2022). Limb development genes underlie variation in human fingerprint patterns. *Cell* **185**, 95-112.e18.

Lin, H. F., Traver, D., Zhu, H., Dooley, K., Paw, B. H., Zon, L. I. and Handin, R. I. (2005). Analysis of thrombocyte development in CD41-GFP transgenic zebrafish. *Blood*.

Long, Q., Meng, A., Wang, M., Jessen, J. R., Farrell, M. J. and Lin, S. (1997). GATA-1 expression pattern can be recapitulated in living transgenic zebrafish using GFP reporter gene. *Development* **124**, 4105–4111.

Love, A. M., Prince, D. J. and Jessen, J. R. (2018). Vangl2-dependent regulation of membrane protrusions and directed migration requires a fibronectin extracellular matrix. *Development* dev.165472.

Lun, A. T. L., Chen, Y. and Smyth, G. K. (2016). It's DE-licious: A Recipe for Differential Expression Analyses of RNA-seq Experiments Using Quasi-Likelihood Methods in edgeR. *Methods Mol. Biol.* **1418**, 391–416.

Marlow, F., Zwartkruis, F., Malicki, J., Neuhauss, S. C. F., Abbas, L., Weaver, M., Driever, W. and Solnica-Krezel, L. (1998). Functional interactions of genes mediating convergent extension, knypek and trilobite, during the partitioning of the eye primordium in zebrafish. *Dev. Biol.* **203**, 382–399.

Marlow, F., Topczewski, J., Sepich, D. and Solnica-Krezel, L. (2002). Zebrafish Rho kinase 2 acts downstream of Wnt11 to mediate cell polarity and effective convergence and extension movements. *Curr. Biol.* **12**, 876–884.

Matsui, T., Raya, Á., Kawakami, Y., Callol-Massot, C., Capdevila, J., Rodríguez-Esteban, C. and Belmonte, J. C. I. (2005). Noncanonical Wnt signaling regulates midline convergence of organ primordia during zebrafisn development. *Genes Dev.*

McMahon, J. J., Miller, E. E. and Silver, D. L. (2016). The exon junction complex in neural development and

neurodevelopmental disease. *Int. J. Dev. Neurosci.*

Merks, A. M., Swinarski, M., Meyer, A. M., Müller, N. V., Özcan, I., Donat, S., Burger, A., Gilbert, S., Mosimann, C., Abdelilah-Seyfried, S., et al. (2018). Planar cell polarity signalling coordinates heart tube remodelling through tissue-scale polarisation of actomyosin activity. *Nat. Commun.* **9**, 2161.

Montague, T. G., Cruz, J. M., Gagnon, J. A., Church, G. M. and Valen, E. (2014). CHOPCHOP: a CRISPR/Cas9 and TALEN web tool for genome editing. *Nucleic Acids Res.* **42**, W401–W407.

Moore, C., Richens, J. L., Hough, Y., Ucanok, D., Malla, S., Sang, F., Chen, Y., Elworthy, S., Wilkinson, R. N. and Gering, M. (2018). Gfi1aa and Gfi1b set the pace for primitive erythroblast differentiation from hemangioblasts in the zebrafish embryo. *Blood Adv.* **2**, 2589–2606.

Mosimann, C., Panáková, D., Werdich, A. A., Musso, G., Burger, A., Lawson, K. L., Carr, L. A., Nevis, K. R., Sabeh, M. K., Zhou, Y., et al. (2015). Chamber identity programs drive early functional partitioning of the heart. *Nat. Commun.* **6**,.

Mugford, J. W., Sipilä, P., Kobayashi, A., Behringer, R. R. and McMahon, A. P. (2008). Hoxd11 specifies a program of metanephric kidney development within the intermediate mesoderm of the mouse embryo. *Dev. Biol.* **319**, 396–405.

Niihori, T., Ouchi-Uchiyama, M., Sasahara, Y., Kaneko, T., Hashii, Y., Irie, M., Sato, A., Saito-Nanjo, Y., Funayama, R., Nagashima, T., et al. (2015). Mutations in MECOM, Encoding Oncoprotein EVI1, Cause Radioulnar Synostosis with Amegakaryocytic Thrombocytopenia. **97**, 848–854.

North, T. E., Goessling, W., Walkley, C. R., Lengerke, C., Kopani, K. R., Lord, A. M., Weber, G. J., Bowman, T. V, Jang, I. H., Grosser, T., et al. (2007). Prostaglandin E2 regulates vertebrate haematopoietic stem cell homeostasis. *Nature* **447**, 1007–1011.

Onimaru, K., Shoguchi, E., Kuratani, S. and Tanaka, M. (2011). Development and evolution of the lateral plate mesoderm: comparative analysis of amphioxus and lamprey with implications for the acquisition of paired fins. *Dev. Biol.* **359**, 124–136.

Orkin, S. H. and Zon, L. I. (2008). Hematopoiesis: an evolving paradigm for stem cell biology. *Cell* **132**, 631–644.

Palacios, I. M., Gatfield, D., St Johnston, D. and Izaurralde, E. (2004). An eIF4AIII-containing complex required for mRNA localization and nonsense-mediated mRNA decay. *Nature* **427**, 753–7.

Panakova, D., Werdich, A. A. and Macrae, C. A. (2010). Wnt11 patterns a myocardial electrical gradient through regulation of the L-type Ca(2+) channel. *Nature* **466**, 874–878.

Pang, H., Yu, X., Kim, Y. M., Wang, X., Jinkins, J. K., Yin, J., Li, S. and Gu, H. (2020). Disorders Associated With Diverse, Recurrent Deletions and Duplications at 1q21.1. *Front. Genet.*

Parmar, K., D'Andrea, A. and Niedernhofer, L. J. (2009). Mouse models of Fanconi anemia. *Mutat. Res.* **668**, 133.

Patro, R., Duggal, G., Love, M. I., Irizarry, R. A. and Kingsford, C. (2017). Salmon provides fast and bias-aware quantification of transcript expression. *Nat. Methods 2017 144* **14**, 417–419.

Patterson, L. T., Pembaur, M. and Potter, S. S. (2001). Hoxa11 and Hoxd11 regulate branching morphogenesis of the ureteric bud in the developing kidney. *Development* **128**, 2153–2161.

Perkins, A. S., Mercer, J. A., Jenkins, N. A. and Copeland, N. G. (1991). Patterns of Evi-1 expression in embryonic and adult tissues suggest that Evi-1 plays an important regulatory role in mouse development. *Development* **111**, 479–487.

Petit, F. and Boussion, S. (2022). Thrombocytopenia Absent Radius Syndrome. *GeneReviews®*.

Pierpont, M. E., Brueckner, M., Chung, W. K., Garg, V., Lacro, R. V., McGuire, A. L., Mital, S., Priest, J. R., Pu, W. T., Roberts, A., et al. (2018). Genetic Basis for Congenital Heart Disease: Revisited: A Scientific Statement From the American Heart Association. *Circulation* **138**,.

Pinho, S. and Frenette, P. S. (2019). *Haematopoietic stem cell activity and interactions with the niche*. Nature Publishing Group.

Prince, D. J. and Jessen, J. R. (2019). Dorsal convergence of gastrula cells requires a Vangl2 and adhesion protein-dependent change in protrusive activity. *Development*.

Prummel, K. D., Nieuwenhuize, S. and Mosimann, C. (2020). The lateral plate mesoderm. **147**,.

Prummel, K. D., Crowell, H. L., Nieuwenhuize, S., Brombacher, E. C., Daetwyler, S., Soneson, C., Kresoja-Rakic, J., Kocere, A., Ronner, M., Ernst, A., et al. (2022). Hand2 delineates mesothelium progenitors and is reactivated in mesothelioma. *Nat. Commun. 2022 131* **13**, 1–21.

Quinlan, A. R. and Hall, I. M. (2010). BEDTools: a flexible suite of utilities for comparing genomic features. *Bioinformatics* **26**, 841–842.

Robinson, M. D., McCarthy, D. J. and Smyth, G. K. (2010). edgeR: a Bioconductor package for differential expression analysis of digital gene expression data. *Bioinformatics* **26**, 139–140.

Roignant, J. Y. and Treisman, J. E. (2010). Exon Junction Complex Subunits Are Required to Splice Drosophila MAP Kinase, a Large Heterochromatic Gene. *Cell* **143**, 238–250.

Roszko, I., Sawada, A. and Solnica-Krezel, L. (2009). Regulation of convergence and extension movements during vertebrate gastrulation by the Wnt/PCP pathway. *Semin. Cell Dev. Biol.* **20**, 986–97.

Roszko, I., Sepich, D. S., Jessen, J. R., Chandrasekhar, A. and Solnica-Krezel, L. (2015). A dynamic intracellular distribution of Vangl2 accompanies cell polarization during zebrafish gastrulation. *Dev.*

Schier, A. F. and Talbot, W. S. (2005). Molecular genetics of axis formation in zebrafish. *Annu Rev Genet* **39**, 561–613.

Schindelin, J., Arganda-Carreras, I., Frise, E., Kaynig, V., Longair, M., Pietzsch, T., Preibisch, S., Rueden, C., Saalfeld, S., Schmid, B., et al. (2012). Fiji: an open-source platform for biological-image analysis. *Nat. Methods* **9**, 676–82.

Schneider, C. A., Rasband, W. S. and Eliceiri, K. W. (2012). NIH Image to ImageJ: 25 years of image analysis. *Nat. Methods* **9**, 671–675.

Schoenwolf, G. C., Garcia-Martinez, V. and Dias, M. S. (1992). Mesoderm movement and fate during avian gastrulation and neurulation. *Dev. Dyn.* **193**, 235–48.

Schulte-Merker, S., Hammerschmidt, M., Beuchle, D., Cho, K. W., De Robertis, E. M. and Nüsslein-Volhard, C. (1994a). Expression of zebrafish goosecoid and no tail gene products in wild-type and mutant no tail embryos. *Development* **120**, 843–852.

Schulte-Merker, S., van Eeden, F. J., Halpern, M. E., Kimmel, C. B. and Nüsslein-Volhard, C. (1994b). no

tail (ntl) is the zebrafish homologue of the mouse T (Brachyury) gene. *Development* **120**, 1009–15.

Shi, H. and Xu, R. M. (2003). Crystal structure of the Drosophila Mago nashi–Y14 complex. *Genes Dev.* **17**, 971–976.

Solnica-Krezel, L., Stemple, D. L., Mountcastle-Shah, E., Rangini, Z., Neuhauss, S. C., Malicki, J., Schier, A. F., Stainier, D. Y., Zwartkruis, F., Abdelilah, S., et al. (1996). Mutations affecting cell fates and cellular rearrangements during gastrulation in zebrafish. *Development* **123**, 67–80.

Soneson, C., Matthes, K. L., Nowicka, M., Law, C. W. and Robinson, M. D. (2016a). Isoform prefiltering improves performance of count-based methods for analysis of differential transcript usage. **17**, 12.

Soneson, C., Love, M. I. and Robinson, M. D. (2016b). Differential analyses for RNA-seq: transcript-level estimates improve gene-level inferences. **4**, 1521.

Stainier, D. Y. R., Raz, E., Lawson, N. D., Ekker, S. C., Burdine, R. D., Eisen, J. S., Ingham, P. W., Schulte-Merker, S., Yelon, D., Weinstein, B. M., et al. (2017). Guidelines for morpholino use in zebrafish. *PLOS Genet.* **13**, e1007000.

Stoll, C., Dott, B., Alembik, Y. and Roth, M. P. (2013). Associated malformations among infants with radial ray deficiency. *Genet. Couns.*

Sugimura, R., He, X. C., Venkatraman, A., Arai, F., Box, A., Semerad, C., Haug, J. S., Peng, L., Zhong, X. B., Suda, T., et al. (2012). Noncanonical Wnt signaling maintains hematopoietic stem cells in the niche. *Cell* **150**, 351–365.

Takamiya, M. and Campos-Ortega, J. A. (2006). Hedgehog signalling controls zebrafish neural keel morphogenesis via its level-dependent effects on neurogenesis. *Dev. Dyn.* **235**, 978–997.

Thambyrajah, R., Ucanok, D., Jalali, M., Hough, Y., Wilkinson, R. N., McMahon, K., Moore, C. and Gering, M. (2016). A gene trap transposon eliminates haematopoietic expression of zebrafish Gfi1aa, but does not interfere with haematopoiesis. *Dev. Biol.* **417**, 25–39.

Thisse, C. and Thisse, B. (2008). High-resolution in situ hybridization to whole-mount zebrafish embryos. *Nat. Protoc.* **3**, 59–69.

Thompson, A. A. and Nguyen, L. T. (2000). Amegakaryocytic thrombocytopenia and radio-ulnar synostosis are associated with HOXA11 mutation. *Nat. Genet. 2000 264* **26**, 397–398.

Thompson, M. A., Ransom, D. G., Pratt, S. J., MacLennan, H., Kieran, M. W., Detrich, H. W., Vail, B., Huber, T. L., Paw, B., Brownlie, A. J., et al. (1998). TheclocheandspadetailGenes Differentially Affect Hematopoiesis and Vasculogenesis. *Dev. Biol.* **197**, 248–269.

Thompson, A. A., Woodruff, K., Feig, S. A., Nguyen, L. T. and Carolyn Schanen, N. (2001). Congenital thrombocytopenia and radio-ulnar synostosis: a new familial syndrome. *Br. J. Haematol.* **113**, 866–870.

Topczewski, J., Sepich, D. S., Myers, D. C., Walker, C., Amores, A., Lele, Z., Hammerschmidt, M., Postlethwait, J. and Solnica-Krezel, L. (2001). The zebrafish glypican knypek controls cell polarity during gastrulation movements of convergent extension. *Dev. Cell* **1**, 251–264.

Turner, D. L. and Weintraub, H. (1994). Expression of achaete-scute homolog 3 in Xenopus embryos converts ectodermal cells to a neural fate. *Genes Dev.* **8**, 1434–1447.

Vogel, A. M. and Gerster, T. (1997). Expression of a zebrafish Cathepsin L gene in anterior mesendoderm

and hatching gland. *Dev. Genes Evol.* 477–479.

Wang, L., Zhang, Y., Zhou, T., Fu, Y. F., Du, T. T., Jin, Y., Chen, Y., Ren, C. G., Peng, X. L., Deng, M., et al. (2008). Functional characterization of Lmo2-Cre transgenic zebrafish. *Dev Dyn* **237**, 2139–2146.

Wang, B., Sinha, T., Jiao, K., Serra, R. and Wang, J. (2011). Disruption of PCP signaling causes limb morphogenesis and skeletal defects and may underlie Robinow syndrome and brachydactyly type B. *Hum. Mol. Genet.* **20**, 271–85.

Wei, W., Wen, L., Huang, P., Zhang, Z., Chen, Y., Xiao, A., Huang, H., Zhu, Z., Zhang, B. and Lin, S. (2008). Gfi1.1 regulates hematopoietic lineage differentiation during zebrafish embryogenesis. *Cell Res.* **18**, 677–685.

Weinberg, E. S., Allende, M. L., Kelly, C. S., Abdelhamid, A., Murakami, T., Andermann, P., Doerre, O. G., Grunwald, D. J. and Riggleman, B. (1996). Developmental regulation of zebrafish MyoD in wild-type, no tail and spadetail embryos. **122**, 271–280.

Westerfield, M. (2007). *The Zebrafish Book: a guide for the laboratory use of zebrafish (Danio rerio)*. 5th ed. Eugene: University of Oregon Press.

Whitfield, T. T., Granato, M., van Eeden, F. J., Schach, U., Brand, M., Furutani-Seiki, M., Haffter, P., Hammerschmidt, M., Heisenberg, C. P., Jiang, Y. J., et al. (1996). Mutations affecting development of the zebrafish inner ear and lateral line. *Development* **123**, 241–54.

Williams, M. L. K. and Solnica-Krezel, L. (2020). Nodal and planar cell polarity signaling cooperate to regulate zebrafish convergence & extension gastrulation movements. *Elife*.

Xing, Y. Y., Cheng, X. N., Li, Y. L., Zhang, C., Saquet, A., Liu, Y. Y., Shao, M. and Shi, D. L. (2018). Mutational analysis of dishevelled genes in zebrafish reveals distinct functions in embryonic patterning and gastrulation cell movements. *PLoS Genet.* **14**,.

Yamanaka, Y., Tamplin, O. J., Beckers, A., Gossler, A. and Rossant, J. (2007). Live imaging and genetic analysis of mouse notochord formation reveals regional morphogenetic mechanisms. *Dev. Cell* **13**, 884–96.

Yang, Y. and Mlodzik, M. (2015). Wnt-Frizzled/Planar Cell Polarity Signaling: Cellular Orientation by Facing the Wind (Wnt). *Annu. Rev. Cell Dev. Biol.* **31**, 623–646.

Yin, C. and Solnica-Krezel, L. (2007). Convergence and extension movements mediate the specification and fate maintenance of zebrafish slow muscle precursors. *Dev. Biol.* **304**, 141–55.

Yokomizo, T., Ideue, T., Morino-Koga, S., Tham, C. Y., Sato, T., Takeda, N., Kubota, Y., Kurokawa, M., Komatsu, N., Ogawa, M., et al. (2022). Independent origins of fetal liver haematopoietic stem and progenitor cells. *Nat. 2022* 1–6.

Yuan, X., Wang, X., Bi, K. and Jiang, G. (2015). The role of EVI-1 in normal hematopoiesis and myeloid malignancies (review). *Int. J. Oncol.* **47**, 2028–2036.

Yzaguirre, A. D., de Bruijn, M. F. T. R. and Speck, N. A. (2017). The role of Runx1 in embryonic blood cell formation. In *Advances in Experimental Medicine and Biology*, .

Zhang, X. Y. and Rodaway, A. R. F. (2007). SCL-GFP transgenic zebrafish: In vivo imaging of blood and endothelial development and identification of the initial site of definitive hematopoiesis. *Dev. Biol.* **307**,

179–194.

Zhang, Y., Gao, S., Xia, J. and Liu, F. (2018). Hematopoietic Hierarchy – An Updated Roadmap. *Trends Cell Biol.*

Zhao, X. F., Nowak, N. J., Shows, T. B. and Aplan, P. D. (2000). MAGOH Interacts with a Novel RNA-Binding Protein. *Genomics* **63**, 145–148.

Zhou, Y., Cashman, T. J., Nevis, K. R., Obregon, P., Carney, S. A., Liu, Y., Gu, A., Mosimann, C., Sondalle, S., Peterson, R. E., et al. (2011). Latent TGF-βbinding protein 3 identifies a second heart field in zebrafish. *Nature* **474**,.

Zhou, Y., Zhou, B., Pache, L., Chang, M., Khodabakhshi, A. H., Tanaseichuk, O., Benner, C. and Chanda, S. K. (2019). Metascape provides a biologist-oriented resource for the analysis of systems-level datasets. *Nat. Commun.* **10**,.

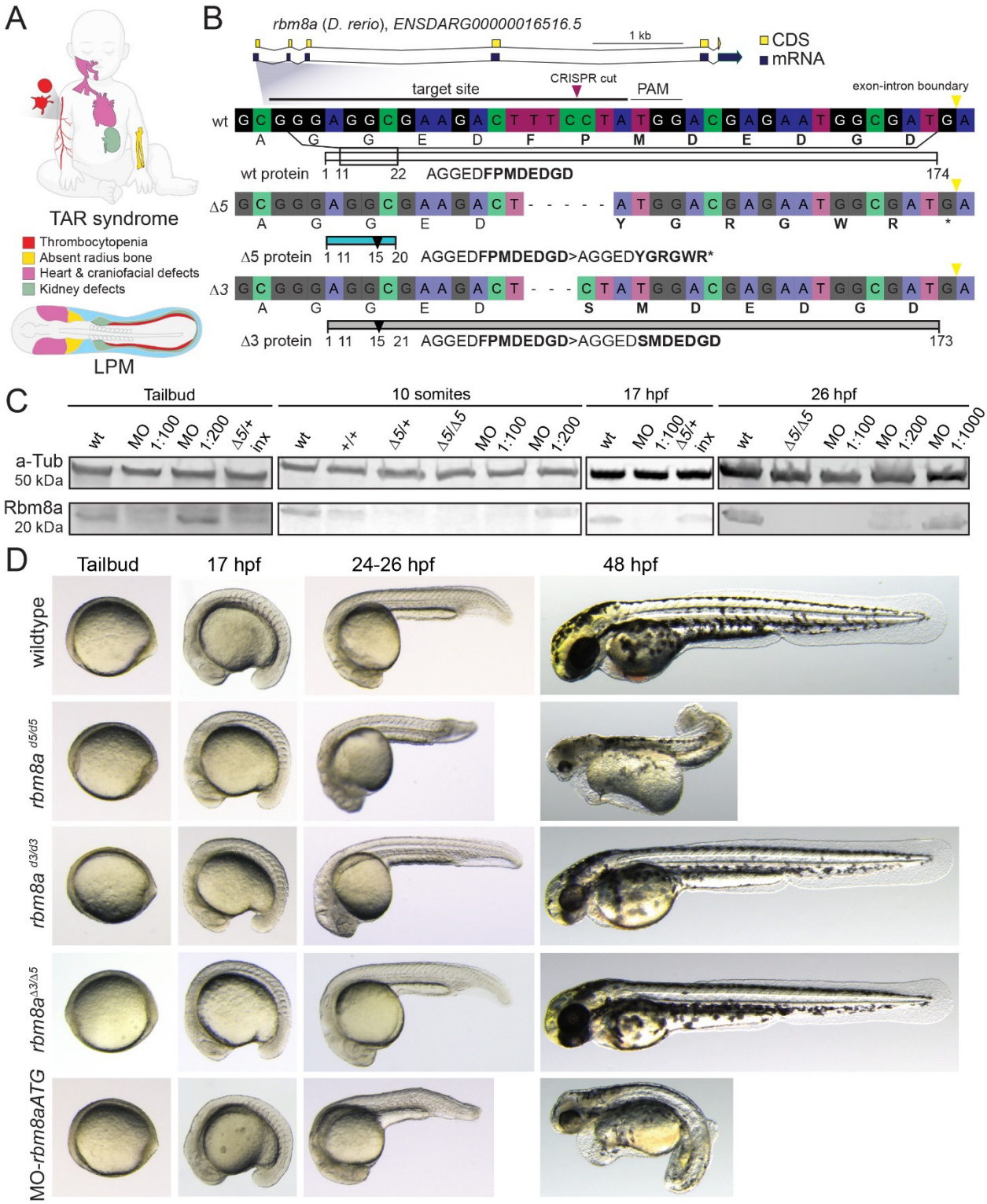

Figure 1: Genetic perturbations in the zebrafish *rbm8a* gene.
(**A**) Hypothesized connection of the human TAR syndrome phenotypes with early lateral plate mesoderm (LPM). Created with Biorender.com. (**B**) Allelic series of *rbm8a* in zebrafish with wildtype allele, *rbm8a*$^{\Delta 5}$ allele and *rbm8a*$^{\Delta 3}$ allele induced by Cas9-mediated mutagenesis. (**C**) Western blot analysis of Rbm8a protein in mutants and morphants at different developmental stages, showing gradual decrease of maternal protein in mutants and translation block in morphants. (**D**) Representative images of zebrafish embryos carrying different *rbm8a* allele combinations during early development. Compared to wildtype and different *rbm8a*$^{\Delta 5}$ and *rbm8a*$^{\Delta 3}$ combinations, homozygous *rbm8a*$^{\Delta 5}$ carriers display severe microcephaly and corkscrew tail phenotype. *rbm8a* morphant (1:100 injection dilution) phenotypically recapitulates the homozygous *rbm8a*$^{\Delta 5}$ embryos.

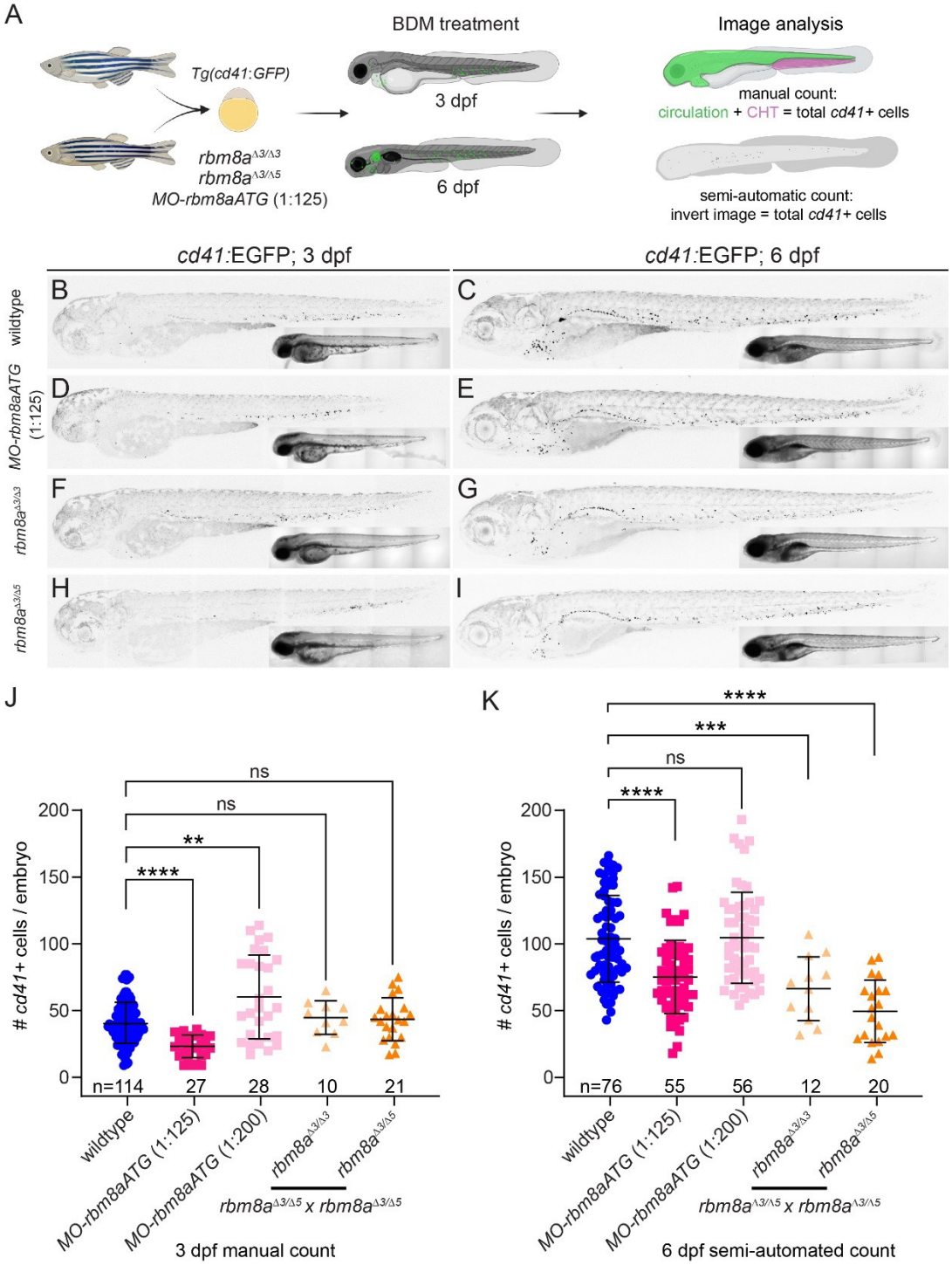

Figure 2: *rbm8a* perturbation reduces thrombocyte numbers in zebrafish larvae.
(**A**) Schematic of the workflow to introduce genetic perturbations in *rbm8a* and to quantify thrombocyte progenitors in circulation and in the caudal hematopoietic territory (CHT). Created with Biorender.com. (**B-I**) Representative confocal images of zebrafish embryos transgenic for the thrombocyte marker *cd41:GFP*, greyscale and color-inverted to reveal GFP-positive cells; anterior to the left, insert depicts brightfield image of larvae for reference. (**J**,**K**) *cd41:*GFP-positive thrombocyte counts at 3 dpf (**J**) and 6 dpf (**K**) for each analyzed condition. Individual datapoints shown with mean and standard deviation, significance by Mann-Whitney test. Wildtype larvae have significantly (p=0.0001) more *cd41*:GFP-positive cells at 3 and 6 days compared to the high morpholino dose (1:125), while lower dose (1:200) remained at wildtype levels (**J**,**K**). At 6 dpf (**K**), viable trans-heterozygous allele combinations for *rbm8a* also show a significant thrombocyte reduction; note that morpholino injections will block translation off maternal mRNA, while mutant combinations will retain maternal mRNA function off the wildtype allele carried by the mother (see Supplemental Table for cross details). Individual datapoints (total number of *cd41:GFP*-positive cells per embryo) shown with mean and standard deviation. Significance calculated by Mann-Whitney test (see Supplemental Table 2 for data details).

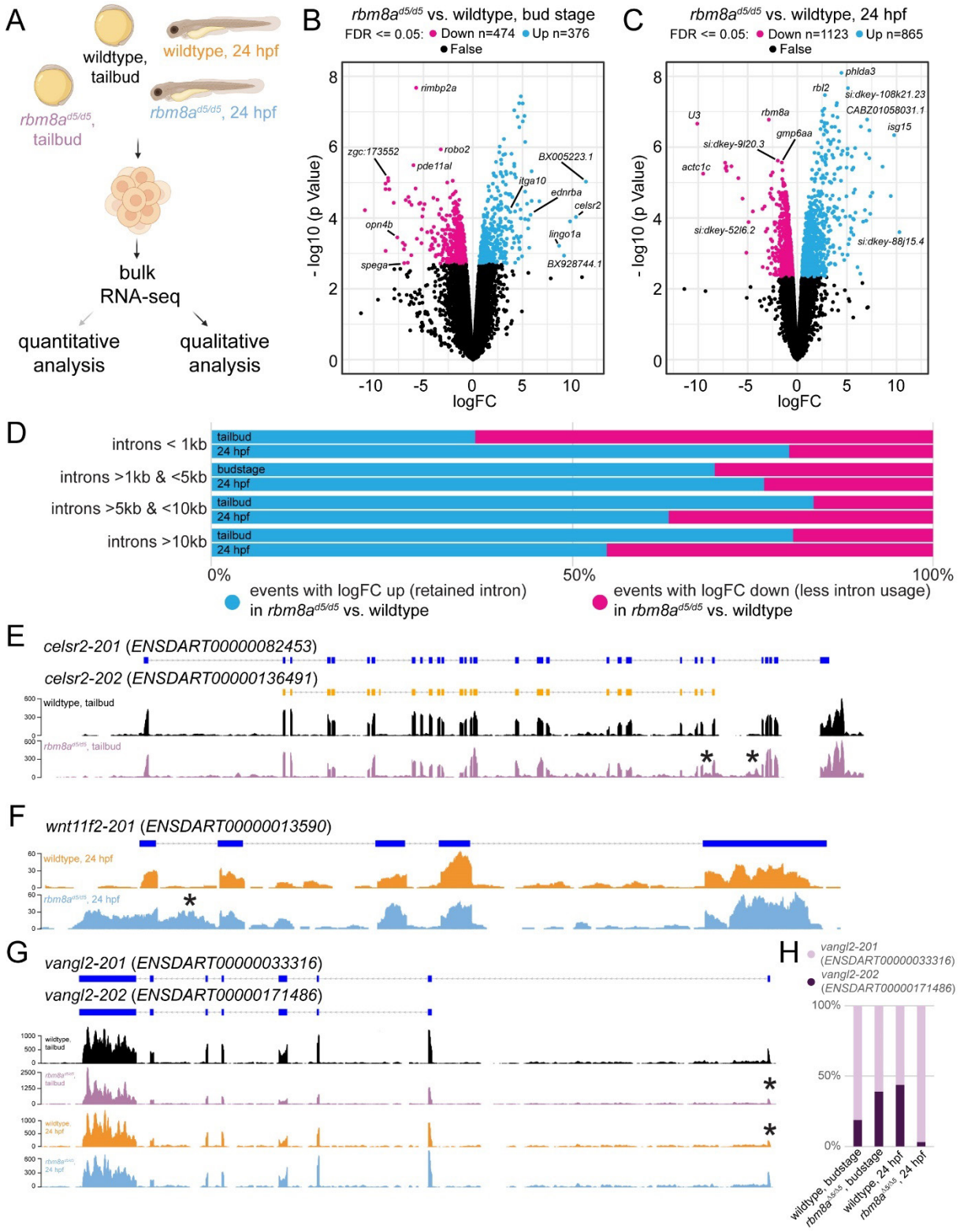

Figure 3: Intron retention in mRNAs encoding non-canonical Wnt/PCP components in zebrafish *rbm8a* mutants.

(**A**) Experimental design of bulk RNA-seq experiment. Created with Biorender.com. (**B**,**C**) Volcano plots of tailbud (B) and 24 hpf (C) comparisons between wildtype versus *rbm8a*-mutant embryos; significantly down- (magenta) and up-regulated (blue) genes with named examples (see Supplemental Tables 3 and 4 for details). (**D**) Qualitative assessment of retained introns between wildtype versus *rbm8a*-mutant embryos; note that retained introns are already apparent at tailbud stage (see Supplemental Table 6 for details). (**E**, **F**) Read coverage plot of mRNA sequencing reads of non-canonical Wnt/PCP components *celsr2*, *wnt11f2* (former *wnt11*), and *vangl2* that feature mRNAs with retained introns (**E**,**F**) and/or differential transcript usage (**G**) in *rbm8a*-mutant embryos. (**H**) Differential transcript usage of *vangl2* transcripts at 24 hpf (exon 1 followed by long intron, asterisks).

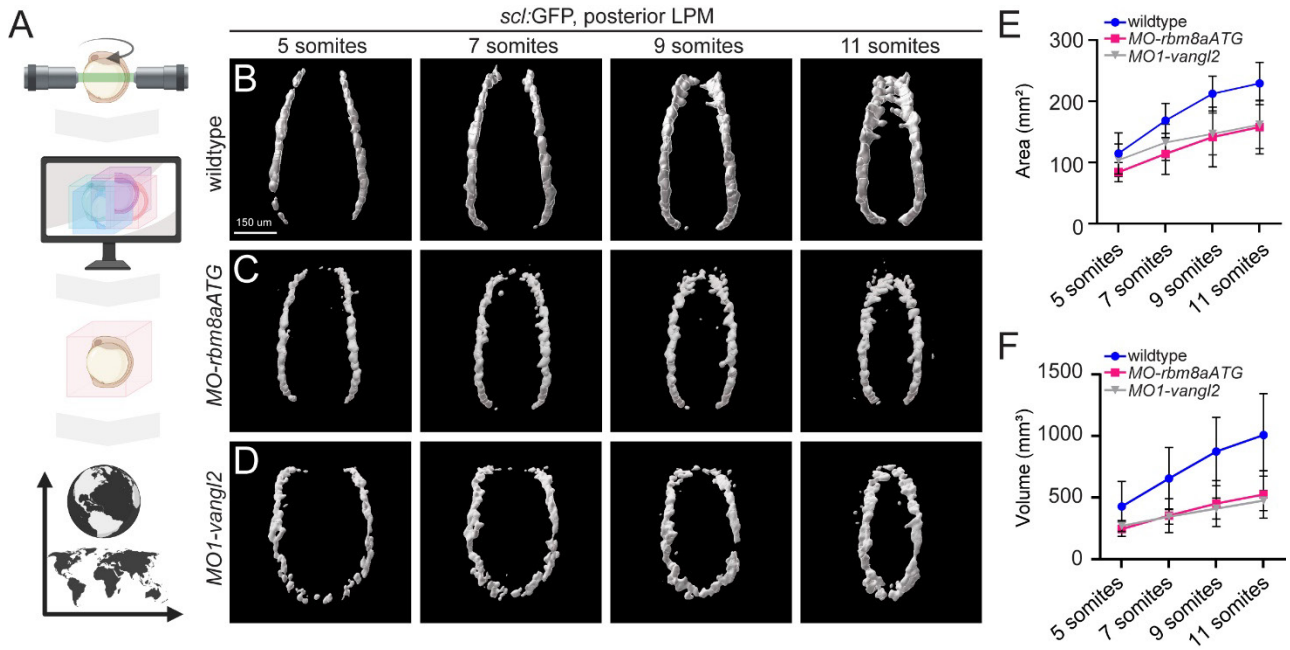

Figure 4: *rbm8a* and *vangl2* perturbations reduce the rate of posterior LPM growth.
(**A**) Schematic of the workflow to image the zebrafish using Light sheet microscope from 4 different angles, assemble in a 3D image and measure volume and area of the PLPM *scl:GFP* surface rendering. Created with Biorender.com. (**B**-**D**) Surface rendering of GFP signal from light sheet-based timelapse imaging of *scl:GFP* transgenic zebrafish embryos. Wildtype (**A**), *rbm8a* morphant (**B**), and *vangl2* morphant (**C**) embryos at 5, 7, 9 and 11 somite stages, dorsal view, anterior to the top, posterior end of the LPM at bottom, scale bar 150 µm. (**D,E**) Area and volume of *scl*:GFP-expressing LPM territory measured with Imaris, comparing wildtype (n=4), *rbm8a* morphant (n=5) and *vangl2* morphant (n=4) measurements depicted in color groups corresponding to sample groups. Note how area in wildtype increases by x^2 (**D**) and volume by x^3 (**E**), revealing reduced growth rates of the posterior *scl*:GFP territory upon *rbm8a* and *vangl2* perturbations. Datapoints shown are mean and standard deviation. 2-way Anova was used to analyze area and volume and both are significantly different in *rbm8a* and *vangl2* mutant embryos compared to wildtype at the analyzed timepoints (see Supplemental Table 8 for data details).

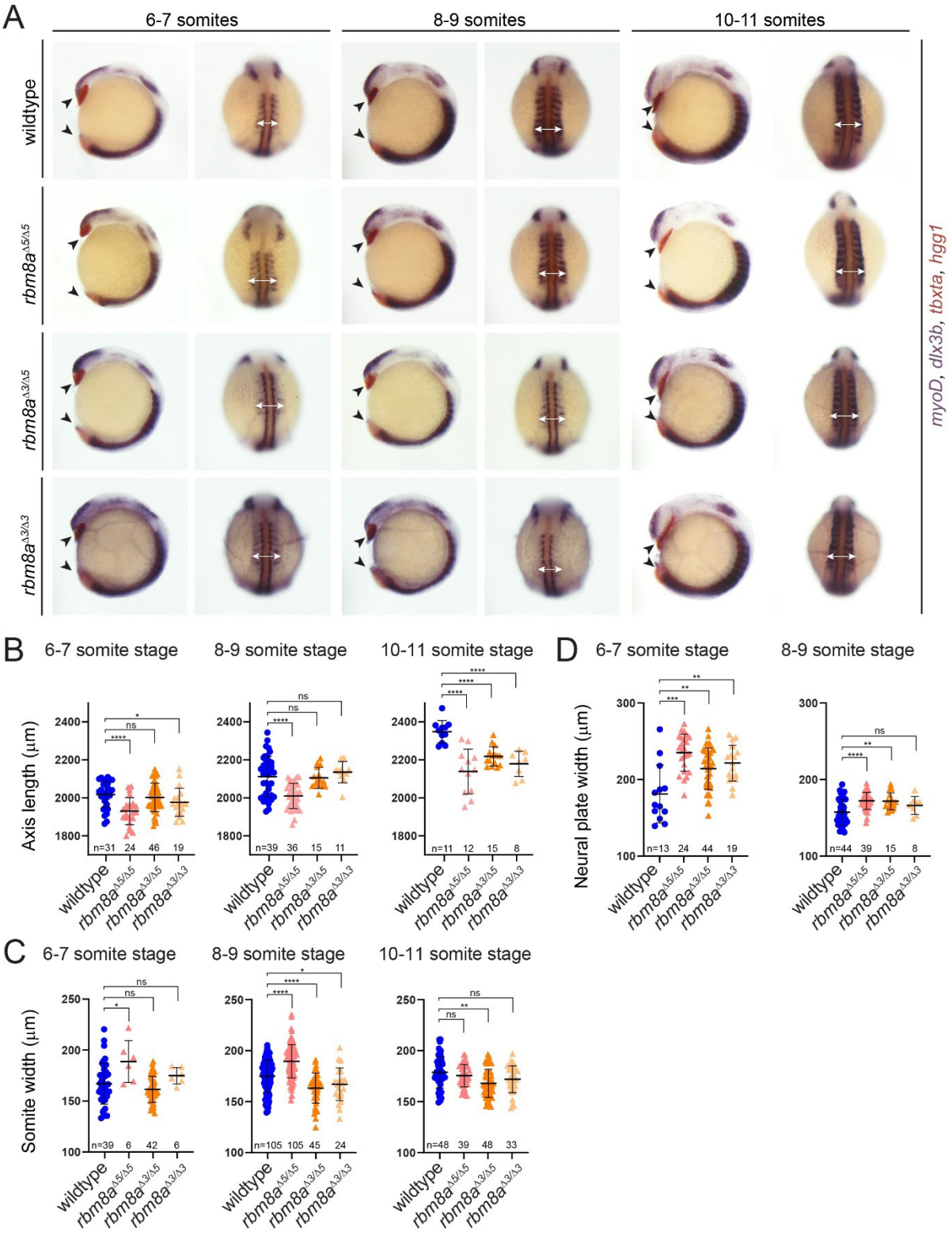

Figure 5: *rbm8a* perturbation results in convergence and extension defects.
(**A**) mRNA *in situ* hybridization for *myoD*, *dlx3b*, *tbxta*, and *hgg1* as landmarks to measure morphometric parameters associated with convergence and extension as influenced by non-canonical Wnt/PCP signaling. Zebrafish embryos are shown as lateral views (odd columns, anterior to the top, ventral to the left) and dorsal views (even columns, anterior to the top). Black arrowheads depict anterior and posterior extent of the body axis in lateral views, white arrows depict somite width at measured position. (**B-D**) Morphometric measurements for axis length (**B**), somite width (**C**), and neural plate (NP) width (**D**) as measured from individual embryo images for each condition. Individual data points shown with median and standard deviation, significance by Mann Whitney test (x column vs y column, see Supplemental Table 9 for data details).

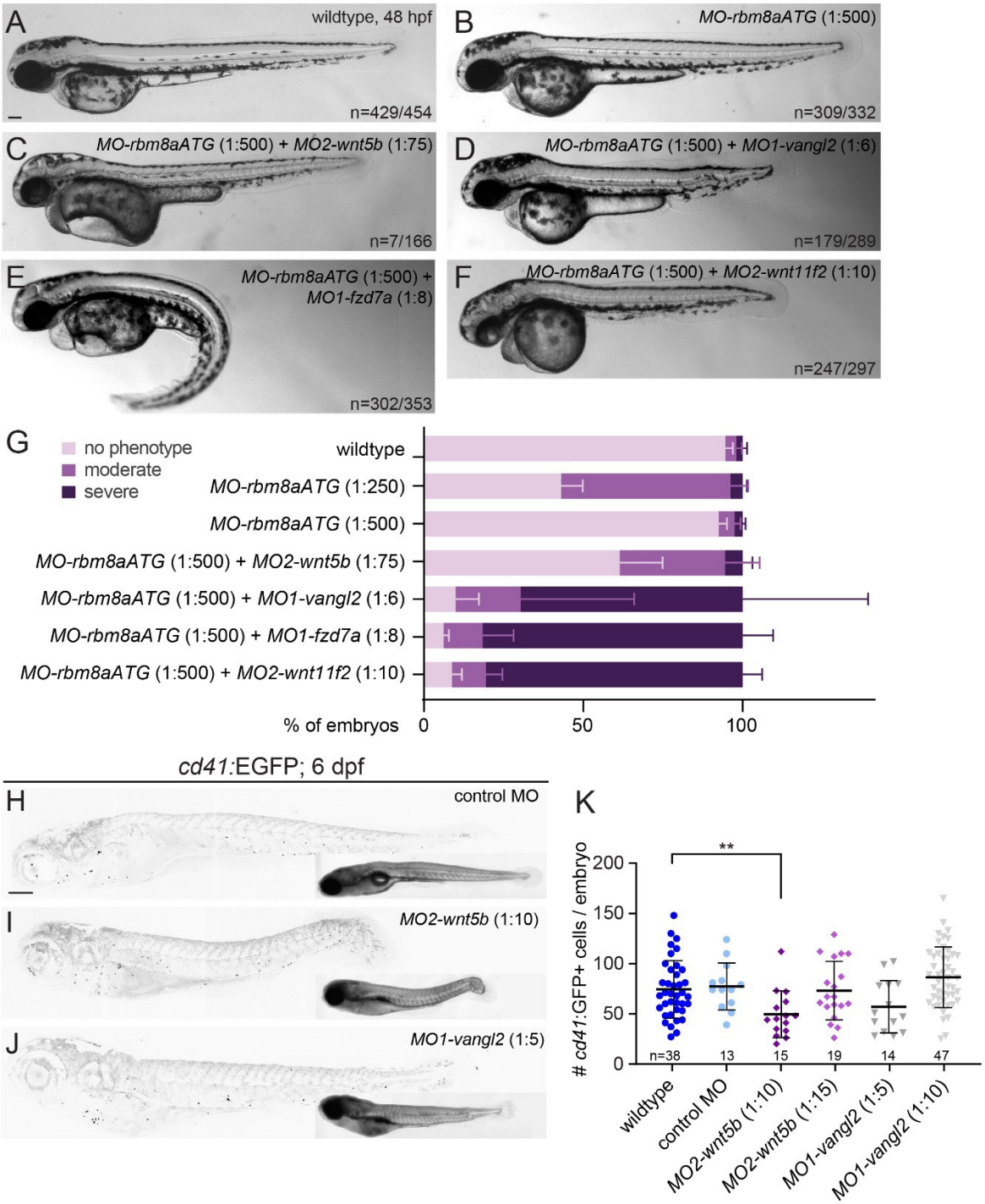

Figure 6: *rbm8a* attenuation sensitizes zebrafish to non-canonical Wnt/PCP defects.
(**A**-**F**) 2 dpf lateral views of representative zebrafish larvae analyzed for each genetic perturbation. Anterior to the left, scalebar 100 µm. (A) Uninjected wildtype as phenotype reference. (**B**) Suboptimal (1:500) *MO-rbm8aATG* injection that does not result in a visible phenotype (as compared to higher doses) and provides a baseline for *rbm8a* attenuation. (**C**-**F**) Representative phenotypes following sequential injection of suboptimal *MO-rbm8aATG* and suboptimal doses of individual, validated morpholinos against the non-canonical Wnt/PCP components *fzd7* (**C**), *vangl2* (**D**), *wnt5b* (**E**), and *wnt11f2* (**F**). (**G**) Observed phenotypes in percent of embryos. (H-K) Reduced function of *vangl2* and *wnt5b* results in reduced *cd41*:GFP-expressing thrombocytes at 6 dpf. (**H**-**J**) Lateral, inverted greyscale views of 6 dpf *cd41:GFP*-transgenic embryos confocal-imaged for GFP fluorescence, inserts depict brightfield view of imaged embryos and overall phenotype reference. Note how suboptimal dosing retains longer viability and less morphological impact (compare to **D**,**E**). (**K**) Thrombocyte quantification at 6 dpf reveals mild, yet dose-dependent reduction in cell number upon *vangl2* and *wnt5b* perturbation. Individual datapoints (total number of *cd41:GFP*-positive cells per embryo) shown with mean and standard deviation, significance by Mann-Whitney test (see Supplemental Table for 10 data details).

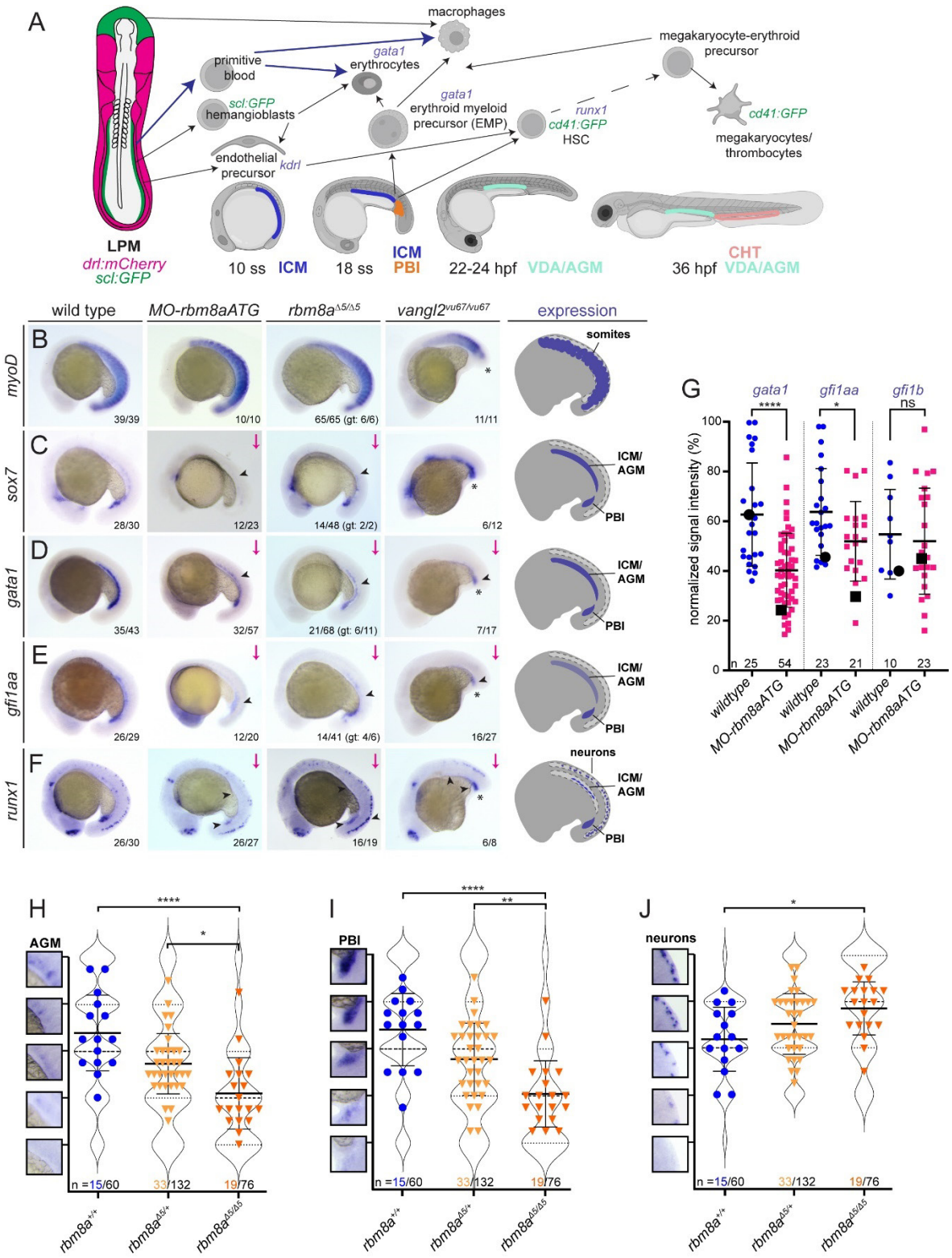

Figure 7: Select changes in hematopoietic marker expression in *rbm8a*- and *vangl2*-mutant zebrafish embryos.

(**A**) Schematic of basic hematopoietic lineage and marker relationships. Created with Biorender.com. (**B-F**) Expression patterns for individual marker genes in wildtype, morpholino-injected, *rbm8a*- and *vangl2*-mutant zebrafish embryos at stage-matched 18 somites. Schematic details areas where marker expression is expected and analyzed. (**B**) *myoD* as marker for somitic muscles shows comparable expression across conditions, with *vangl2* mutants depicting the short, deteriorating tail typical for these mutants (asterisk). (**C**) The early endothelial marker *sox7* is reduced in the trunk upon *rbm8a* perturbation (arrowheads) and seemingly normal in *vangl2* mutants (asterisk). (**D**) The erythroid marker *gata1* is reduced in all *rbm8a*-perturbed embryo conditions (arrowheads) and only retained in posterior-most LPM cells of *vangl2* mutants (asterisk). (**E**) The hematopoietic progenitor marker *gfi1aa* is reduced in

all *rbm8a*-perturbed embryo conditions (arrowheads) and barely detectable in *vangl2*-mutant embryos (asterisk). (**F**) The hematopoietic progenitor marker *runx1* in *rbm8a* morphants and mutants is reduced or absent in the trunk and posterior blood island (PBI) (embryo midline, future dorsal aorta, arrowheads); *vangl2* mutants also show reduced trunk expression (arrowhead) yet retain PBI *runx1* expression (asterisk). (**G**) mRNA *in situ* hybridization-based quantification of *gata1*, *gfi1aa*, and *gfi1b* expression levels; individual data points (normalized signal intensity/embryo) shown with median and standard deviation, significance by Mann-Whitney test. *wt gata1* SD=20.77, MO-*rbm8a*ATG *gata1* SD=14.85, ****<0.000. wt *gfi1aa* SD=17.46, MO-*gfi1aa*ATG SD=16.02, *=0.0310. wt *gfi1b* SD=18.00, MO-*gfi1b*ATG SD=21.32, ns=0.7727. (**I**-**K**) mRNA *in situ* hybridization-based quantification of *runx1* in select areas (AGM (embryo midline, future dorsal aorta), PBI, neurons). (**H**) Signal in AGM. (**I**) Signal in PBI. (**J**) Signal in dorsal neurons. Individual data points (average of 4 scores per embryo) shown with median and standard deviation, significance by Kruskal-Wallis test. Violin plot in background depicts population of the not averaged scores. n numbers = average/total. See Supplemental Table 11 for data details.

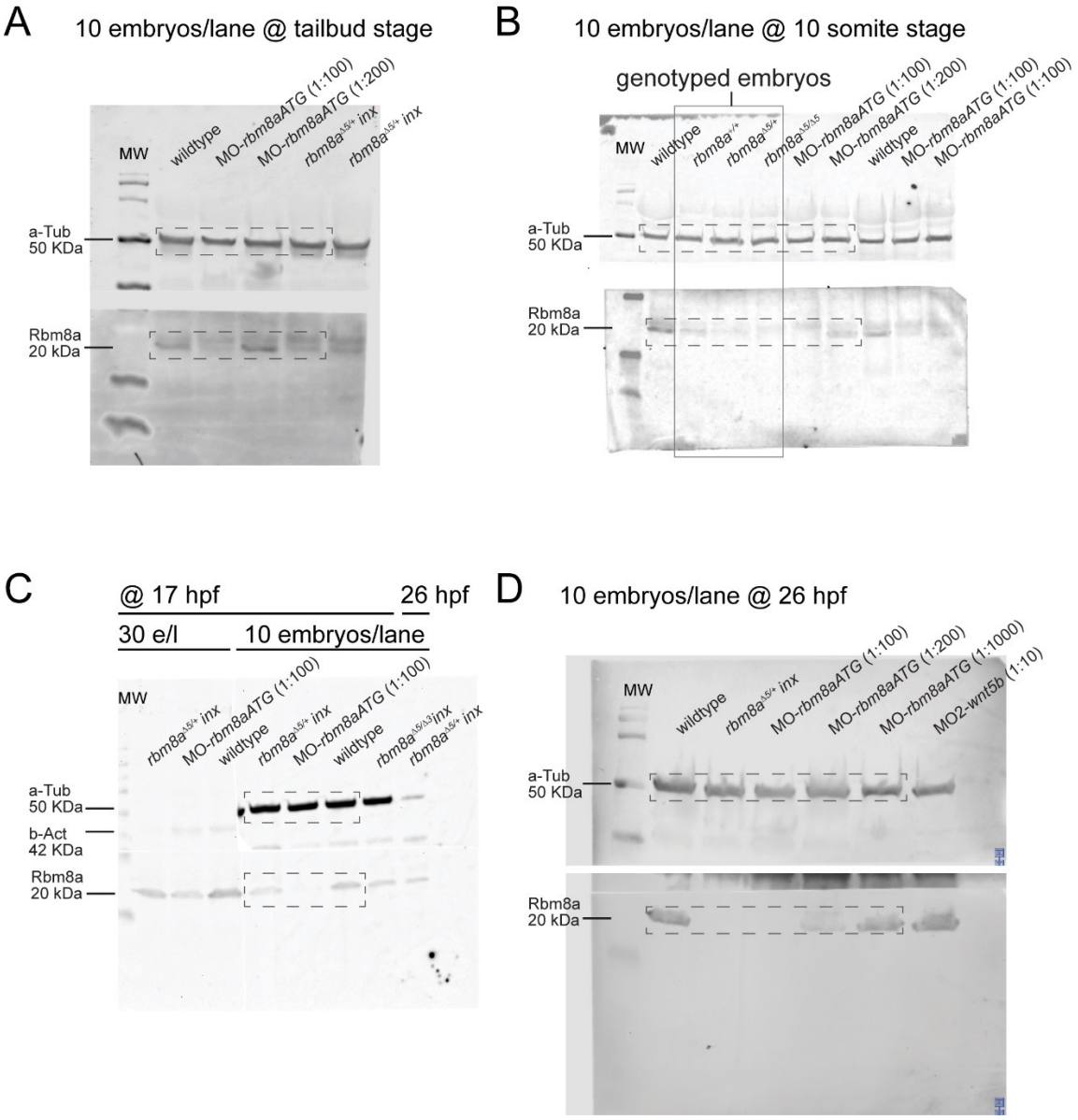

Supplemental Figure 1: Uncropped images of western blots displayed in Fig 1B.
(**A**-**D**) lane 1 MW and 20 kDa Rbm8a antibody. Dashed lines represent frames included in Fig 1B. (**A**) 10 tailbud stage embryos per well. Loading control 50 kDa a-Tubulin. (**B**) 10 10-somite stage embryos per lane. Loading control 50 kDa a-Tubulin. Frame separates lanes 3-5 with *rbm8a* mutant embryos genotyped individually prior to pooling 10 embryos of respective genotype and performing western blot. (**C**) Lanes 2-4 30 17 hpf embryos per lane, loading control 42 kDa b-Actin, lanes 5-9 10 17 hpf embryos per lane, lane 10 10 26 hpf embryos per lane, lanes 5-10 loading control 50 kDa a-Tubulin. (**D**) 10 26 hpf embryos per lane. Loading control 50 kDa a-Tubulin.

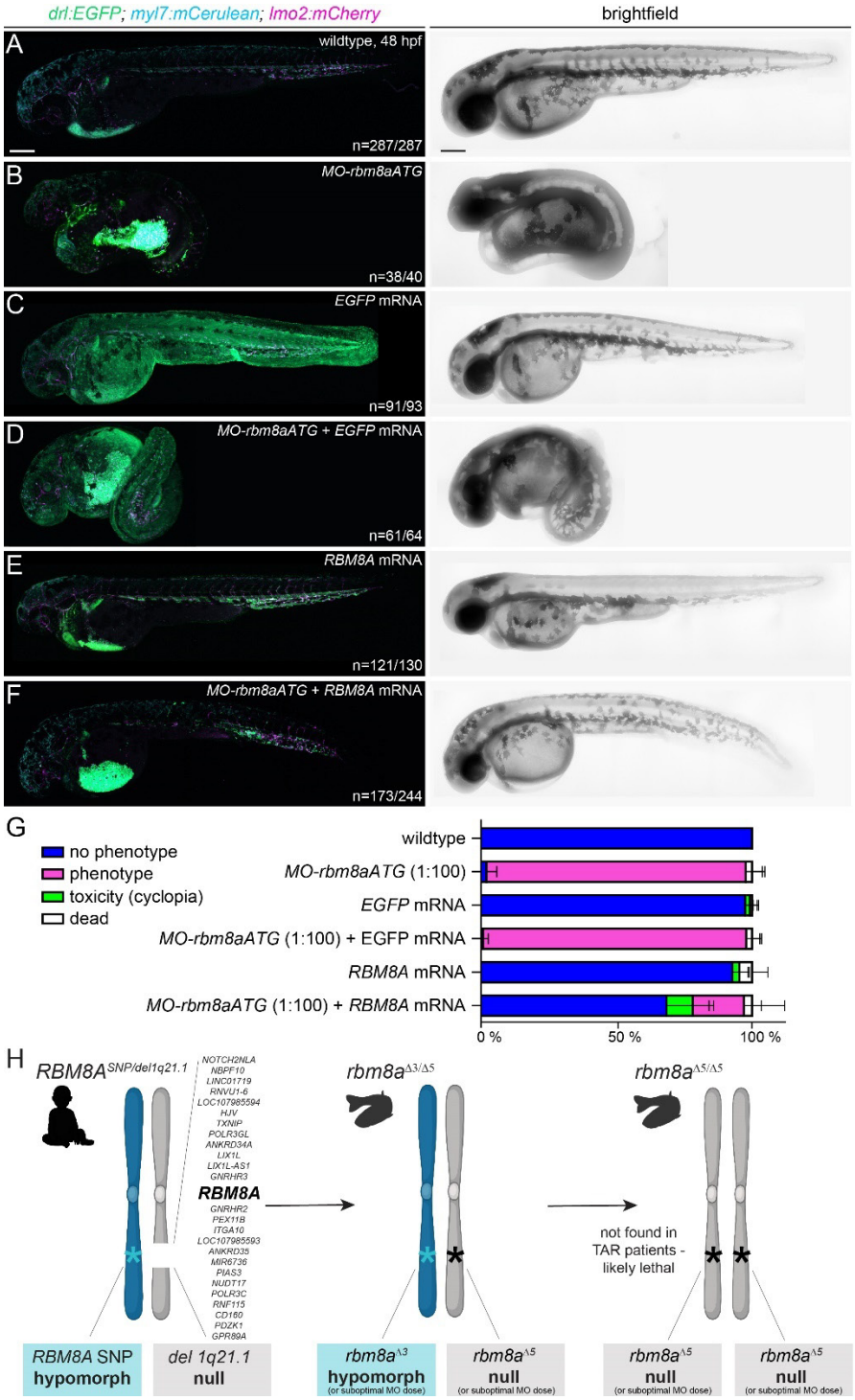

Supplemental Figure 2: Human *RBM8A* mRNA rescues the morpholino phenotype.
(**A**-**F**) Representative confocal images of *drl:EGFP; myl7:mCerulean;lmo2:mCherry* wildtype, morphant, rescued and control injected zebrafish embryos at 48 hpf with brightfield images for reference on the right. Scalebar 200 µm. (**A**) Representative image of wildtype embryo. (**B**) Representative image of MO-*rbm8a*ATG injected embryo. (**C**) Representative image of *EGFP* mRNA injected control embryo. (**D**) Representative image of MO-*rbm8a*ATG and *EGFP* mRNA co-injected control embryo. (**E**) Representative image of *RBM8A* mRNA injected control embryo. (**F**) Representative image of MO-*rbm8a*ATG and *RBM8A* mRNA co-injected (rescued) embryo. (**G**) Overview of rescue n-numbers. Note how nearly 100% of MO-*rbm8a*ATG groups and only ¼ of the rescued embryos have phenotype. Datapoints (%) shown with mean and standard deviation (see Supplemental Table 1 for details). (**H**) Compound heterozygosity for *1q21.1* microdeletions and polymorphisms in human *RBM8A* as observed in TAR syndrome patients, and *rbm8a* mutant allele combinations in zebrafish. Created with Biorender.com.

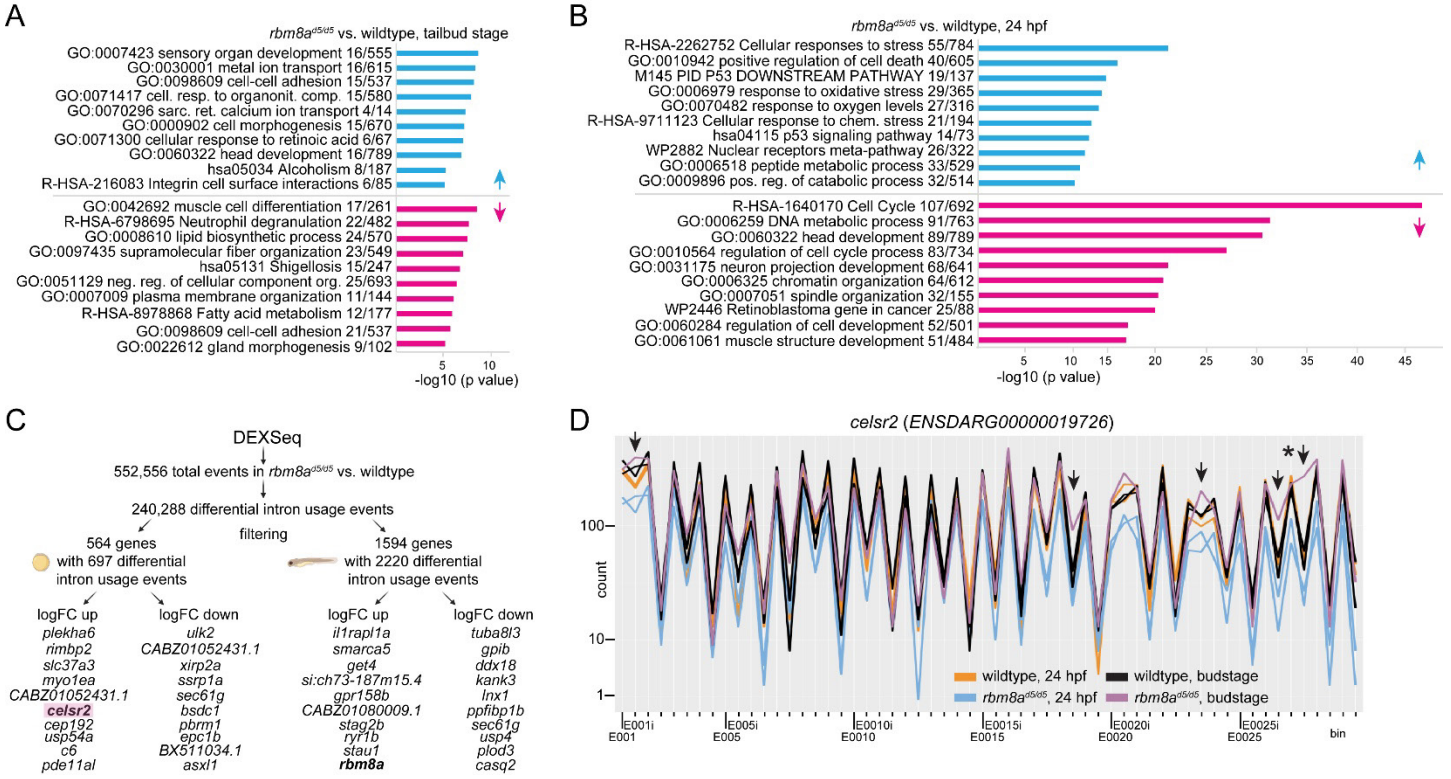

Supplemental Figure 3: Quantitative and qualitative transcriptome analysis of zebrafish *rbm8a* mutants. (**A,B**) Disrupted (up- and down-regulated) pathways and processes in rbm8a-mutant zebrafish embryos at tailbud stage (**A**) and at 24 hpf (**B**); blue indicates upregulation, magenta indicates downregulation (corresponding arrowheads). (**C**,**D**) DEXSeq analysis to identify genes with differential intron usage reveals transcripts with defects that are retained in rbm8a-mutant embryos. Workflow of the analysis, output, and top altered genes (see Supplemental Table 7 and 8 for details) (**C**), with read count plot for *celsr2* (**D**) as representative gene that shows retained intron events; arrowheads indicate increased intron reads, asterisk indicates majority of transcript with retained individual intron.

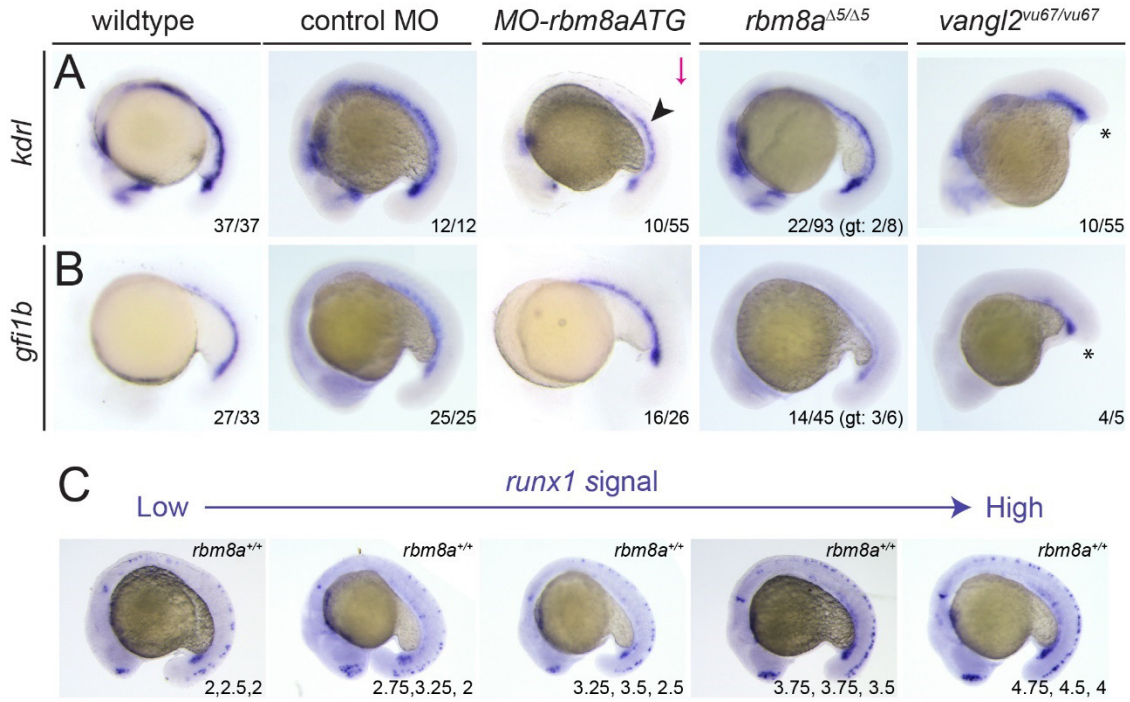

Supplemental Figure 4: Additional mRNA *in situ* hybridization for hematopoietic and endothelial progenitor markers.
(**A, B**) Expression patterns for *kdrl* and *gfi1b* marker genes in wildtype, morpholino-injected, *rbm8a*-mutant, and *vangl2*-mutant zebrafish embryos at 18 somite stage (stage-matched). (**C**) representative scale of *runx1* signal ranked from low to high in *rbm8a* wildtype siblings. Numbers on the bottom represent average score for AGM, PBI and neurons, respectively.

Supplemental Data File:
Raw data of all quantifications in this study includes the following Supplemental Tables:
Supplemental Table 1: Rescue raw data for Supplemental Fig. 2 A-G
Supplemental Table 2: cd41 counts raw data for Fig. 2 J,K
Supplemental Table 3: Differential gene expression (DGE) results filtered budstage for Fig. 3B
Supplemental Table 4: Differential gene expression (DGE) results filtered budstage for Fig. 3C
Supplemental Table 5: Metascape results for Supplemental Fig.3A,B
Supplemental Table 6: DEXSeq results filtered differential intron usage for Fig. 3
Supplemental Table 7: DEXSeq results filtered differential exon usage for Fig. 3
Supplemental Table 8: SPIM area and volume raw data for Fig. 4
Supplemental Table 9: Axis somite neural plate measurements for Fig. 5
Supplemental Table 10: MO coinjection and phenotype analysis raw data for Fig. 6
Supplemental Table 11: ISH signal intensity of Fig. 7